AD-A113 135   MARYLAND UNIV COLLEGE PARK DEPT OF METEOROLOGY   F/G 4/2
OPTIMAL SPATIAL REPRESENTATIONS FOR NUMERICAL WEATHER PREDICTIO--ETC(U)
JAN 82   F BAER, P - SHEU   F19628-78-C-0134
UNCLASSIFIED   AFGL-TR-82-0028   NL

1 OF 1
AD
A113 135

END
DATE
FILMED
5-82
DTIC

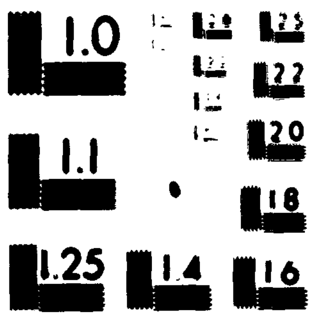
1.0
2.5
2.2
2.0
1.1
1.8
1.25
1.4
1.6

(11)

AFGL-TR-82-0028

OPTIMAL SPATIAL REPRESENTATIONS FOR NUMERICAL WEATHER PREDICTION MODELS BASED ON NORMAL MODE ANALYSES

F. Baer
P. -J. Sheu

Department of Meteorology
University of Maryland
College Park, Maryland 20742

Final Report
June 1978 - September 1981

January 1982

AIR FORCE GEOPHYSICS LABORATORY
AIR FORCE SYSTEMS COMMAND
UNITED STATES AIR FORCE
HANSCOM AFB, MASSACHUSETTS 01731

Unclassified

SECURITY CLASSIFICATION OF THIS PAGE (When Data Entered)

REPORT DOCUMENTATION PAGE	READ INSTRUCTIONS BEFORE COMPLETING FORM
1. REPORT NUMBER: AFGL-TR-82-0028 / 2. GOVT ACCESSION NO.	3. RECIPIENT'S CATALOG NUMBER
4. TITLE (and Subtitle): OPTIMAL SPATIAL REPRESENTATIONS FOR NUMERICAL WEATHER PREDICTION MODELS BASED ON NORMAL MODE ANALYSES	5. TYPE OF REPORT & PERIOD COVERED: Final Report, June 1978 - September 198
	6. PERFORMING ORG. REPORT NUMBER
7. AUTHOR(s): F. Baer, F.-J. Shew	8. CONTRACT OR GRANT NUMBER(s): F19628-78-C-0134
9. PERFORMING ORGANIZATION NAME AND ADDRESS: Department of Meteorology, University of Maryland, College Park, Maryland 20742	10. PROGRAM ELEMENT, PROJECT, TASK AREA & WORK UNIT NUMBERS: 61102F, 2310G2AJ
11. CONTROLLING OFFICE NAME AND ADDRESS: Air Force Geophysics Laboratory, Hanscom AFB, Massachusetts 01731, Monitor/Samuel Yee/LYP	12. REPORT DATE: January 1982
	13. NUMBER OF PAGES: 90
14. MONITORING AGENCY NAME & ADDRESS (if different from Controlling Office)	15. SECURITY CLASS. (of this report): Unclassified
	15a. DECLASSIFICATION/DOWNGRADING SCHEDULE

16. DISTRIBUTION STATEMENT (of this Report)

Approved for public release; distribution unlimited

17. DISTRIBUTION STATEMENT (of the abstract entered in Block 20, if different from Report)

18. SUPPLEMENTARY NOTES

19. KEY WORDS (Continue on reverse side if necessary and identify by block number)

1. numerical weather prediction
2. computational modes
3. normal modes analysis
4. fourth-order differencing
5. finite-element method
6. initialization
7. shooting-method

20. ABSTRACT (Continue on reverse side if necessary and identify by block number)

A method is devised to determine the computational er[illegible] associated with space truncation in numerical weather prediction models. This method is based on evaluating the normal modes of the linearized form of the prediction model. The modes are separated into their physical and computational parts. A special procedure has been devised to make this separation definitive. It is the computational modes which give rise to computational

DD FORM 1473

Unclassified

SECURITY CLASSIFICATION OF THIS PAGE (When Data Entered)

20.

errors. To reduce the impact of these modes, their contributions are filtered out of the initial data used to begin a forecast. Although computational mode amplitude will develop during integration because of nonlinearity, the impact of the computational errors can be controlled by the filtering technique described here. If initial filtering is not adequate, additional filtering may be applied periodically throughout the integration period.

CONTENTS

6

1. Introduction

Our ultimate goal in this research effort is to give some definitive information on the quality of various accepted numerical schemes for solving the atmospheric prediction problem and to hopefully show which method is "best". If such a "best" method is not readily available or depends on conditions too varied to be realizeable, we hope at least to describe a technique which might be employed to indicate the best working numerical system under special circumstances.

The issues associated with numerical solution of the atmospheric prediction problem are too broad to be searched in one comprehensive research effort, and specific items must be addressed individually. For example, with reference to the transformation of differential equations to difference form so that numerical integrations can be performed, one must consider both space and time truncation, topics which are significantly different from one another. Moreover, they cannot be discussed without either boundary or initial conditions, respectively, as separate but interwoven problems. We have chosen to focus on the space truncation problem and have presumed a reasonably successful time truncation format. This choice does not imply the importance of one problem over the other, but clearly indicates our research direction and the importance we place on space truncation. We have indeed considered the interface between time and space truncation by studying the split-explicit integration scheme (see Gadd, [illegible]).

Having chosen to study space truncation, we are immediately

faced with additional complexities. For one, the impact of space differencing varies depending on the dimension considered. Thus vertical differences in atmospheric models produce different responses than do horizontal differences. Furthermore, depending on a model's construction, the numerical schemes applied could yield different solutions.

It is evident that a particular model must be chosen for study, some significant numerical schemes must be used for experimentation, some dimensional focus must be established, and a rational method for quality testing must be employed. To present a well defined problem, we have chosen to test numerical schemes on a global atmospheric model which includes most dynamic phenomena, but is not forced. Since forcing plays an independent role in modeling, it is important to establish the evaluation of a homogeneous model (unforced) before the addition of various stimuli (external forces). Additionally, it is found that variations in vertical differencing do not produce changes as dramatic as those found in varying horizontal differencing; consequently we will focus our attention on horizontal differencing. Finally, since [illegible] may be represented [illegible] most atmospheric models, we will concentrate our [illegible] and analysis [illegible] model [illegible] to [illegible] horizontal differencing [illegible]. We have also employed the [illegible] atmosphere, [illegible] and that [illegible].

The most [illegible] numerical methods in use today, based on

years of experience and practice by the numerical prediction community, all stem from a general theme. In particular, those most favored are a 4th-order differencing scheme (currently in use in the GLAS model), a finite-element scheme (tested by Staniforth and Daley (1977) and others) and of course the spectral method. We have chosen to compare results of integrations for the differencing schemes noted above, i.e., 4th order and finite-element, and both will be applied to latitudinal differencing only. For simplicity we shall choose second order differencing to describe the vertical structure of our model.

We come now to the critical question of how these methods may best be compared. Recent developments in normal-mode analysis suggest a systematic procedure, see, for example, Williamson (1976a, 1976b), Williamson and Dickinson (1976). Application of normal mode theory to models has isolated the various wave motions in models and has given insight into procedures for filtering out unwanted (gravity-inertia) waves. This technique is now well established and documented in the literature, see for example, Baer (1977), Machenhauer (1977), Daley (1980), etc. In the process of establishing model modes, computational modes have also been observed; see, for example, Dickinson and Williamson (1972). It is these modes which undoubtedly interfere with the time evolution of true physical modes and thus should be examined. Consequently, the following plan for most effectively studying the impact of various numerical methods on model equations evolved, and will be used to identify the computational impact on numerical integrations.

The linear form of the GLAS (nonforced) model was converted to numerical form by (a) transforming vertical variations using second order differencing; by (b) Fourier transforming longitudinal variations; and by (c) searching out the normal modes in latitude, based on both the fourth-order difference scheme and the finite-element scheme. These modes are carefully sorted into their physical and computational contributions and as noted above, depend on the vertical structure as well as the planetary waves. A detailed procedure is outlined and used to accomplish this task.

The proposed routine to test for the influence of computational modes on numerical integrations of our model, is to filter these modes out of the system. The most effective way to accomplish such filtering is to remove the modes directly from the system. Unfortunately, this would require solving the differential equations in mode space, a tactic not computationally realistic for large models. Alternatively, the contributions to the computational modes may be filtered from the initial data, thereby at least initiating the integration without computational mode amplitude. Because of nonlinearity, these modes may develop with time. This development may be inhibited by periodic filtering of the data during the integration period. Alternatively one could impose constraints on the initial data so that the time derivatives of the data also show no contributions in terms of computational modes. Such a procedure, although elegant in concept, may prove unrealistic in practice. The alternative procedure would impose adjustments on the initial

conditions which could seriously distort the filtered initial data and perhaps cause them to be nonrepresentative of the actual observations. To avoid this pitfall (which has been experienced while filtering gravity modes), we project initial data onto the modes of the difference equations and filter out only the computational modes. We then proceed to the numerical integration with the filtered initial conditions. These integrations are then compared to those performed with no filtering of the initial data. Comparisons of these integrations should show clearly the impact of the computational modes on the evolution of the flow as predicted by the model equations. Furthermore, careful monitoring of the computational modes as they evolve during the nonlinear integration will give detailed insight into their properties and how they affect the atmospheric prediction problem.

[illegible] The Model

A basic primitive equation model will be used to test the numerical procedures to be evaluated in our program. Such a general model was presented by Somerville et al. (1974) in [illegible] coordinates and a version was [illegible] by us. Since we are concerned with computational characteristics, a non-forced model was adopted, with [illegible] geometry and [illegible]. To isolate the critical computational features, the longitudinal distribution was represented spectrally (Fourier series), thereby concentrating primary attention on the latitudinal structure. To establish the computational modes, the model is linearized about

a state of rest. These features will become evident in the subsequent development.

The momentum equation is written in conventional notation as,

$$\frac{\partial \mathbf{V}}{\partial t} + \nabla \cdot \ldots \mathbf{V} + f\mathbf{k} \times \mathbf{V} = -\ldots \quad \text{[illegible]} \qquad (1)$$

and the pressure is defined in terms of the surface pressure p_s, the top pressure (fixed) p_t, and the new independent variable σ,

$$p = p_t + \sigma\pi, \quad \pi = p_s - p_t \qquad (2).$$

In this system, the continuity equation becomes

$$\text{[illegible]} \qquad (3)$$

and the hydrostatic condition may be expressed as

$$\text{[illegible]} \qquad (4).$$

Finally the adiabatic state may be described by the first law of thermodynamics:

$$\text{[illegible]} \qquad (5).$$

As noted above, this system may be linearized about a state of rest. For this purpose we may define mean values which represent the equilibrium of the ground state and perturbation quantities which oscillate about this state. We therefore define the following variables:

$$\pi = \pi(x,y,t)+\bar{\Pi}$$
$$s = s(x,y,\theta,t)+A(\theta)$$
$$\omega = \dot{\theta} + \frac{\theta}{\bar{\Pi}}\frac{\partial \pi}{\partial t} \qquad (6).$$
$$\bar{V} = (u,v)$$
$$\Phi = \phi(x,y,\theta,t) + \bar{\Phi}(\theta)$$
$$\psi = \phi + \theta A \pi$$

Note that $\bar{\Pi} \gg \pi$, $A \gg s$ and $\bar{\Phi} \gg \phi$. Linearizing (1-5) and including the definitions (6), we get the following system of equations:

$$\frac{\partial \bar{V}}{\partial t} + f\hat{k} \times \bar{V} + \nabla_{\theta}\psi = 0$$

$$\frac{\partial^2 \psi}{\partial t\,\partial \theta} + N^2(\theta)\omega = 0 \qquad (7)$$

$$\nabla_{\theta}\cdot\bar{V} + \frac{\partial \omega}{\partial \theta} = 0$$

where N is the Brunt-Vaisala frequency dependent only on the basic (zero-order) structure of the thermal field; it is defined as,

$$N^2 = -A\bar{\Pi}\frac{\partial(\ln s)}{\partial \theta} = -A\bar{\Pi}\left(\frac{C_v}{C_p}\frac{1}{\theta} + \frac{1}{A}\frac{\partial A}{\partial \theta}\right) \qquad (7a).$$

The derivation of the second of equations (7) is given in Appendix A.

System (7) may be simplified further by assuming periodicity in longitude using the functional form $e^{im\lambda}$, where m represents a wave number and λ describes longitude. Because of linearity, the longitudinal dependence disappears from (7) with the introduction of this representation, and the resulting equations have the following form:

$$\frac{\partial u}{\partial t} - fv + \frac{im\phi}{a\cos\theta} = 0$$

$$\frac{\partial v}{\partial t} + fu + \frac{\partial \phi}{\partial y} = 0 \tag{8}$$

$$\frac{imu}{a\cos\theta} + \frac{1}{\cos\theta}\frac{\partial (v\cos\theta)}{\partial y} + \frac{\partial w}{\partial z} = 0$$

$$\frac{\partial^2 \phi}{\partial t\,\partial z} + N^2 w = 0$$

System (8) depends on latitude (θ) or the variable $y = a\theta$, on the vertical variable z, and on time. Since our effort is primarily focused on horizontal space truncation, we have chosen a second-order difference scheme to separate the vertical dependence from latitude and time. Numerous studies in the literature indicate that computations are not as sensitive to vertical truncation as they are to horizontal truncation. Moreover, these two issues are sufficiently distinct so that they may be studied independently.

2.1 Vertical modes

Since the first of eqs. (7) does not involve any vertical derivative, velocity and height fields may be represented by the same vertical structure, say C, and can be separated out directly and completely. Let us replace $\vec V$, ϕ and w with $\vec V C$, ϕC and wW in Eqs. (7), where W is the vertical structure function for vertical motion. $\vec V$, ϕ and w now represent functions of latitude and time only. The last two equations of (7) take the form,

$$C\nabla_r \cdot \vec V + w\frac{\partial W}{\partial z} = 0 \qquad (9),$$

$$\frac{\partial C}{\partial z}\frac{\partial \phi}{\partial t} + wN^2 W = 0$$

Operating with $\frac{\partial}{\partial z}$ on the first of eqs. (9), $\frac{\partial C}{\partial z}$ and w can be removed to form

$$\frac{\frac{\partial \phi}{\partial t}}{\nabla_r \cdot \vec V} = \frac{N^2 W}{\frac{\partial^2 W}{\partial z^2}} = -c^2 ,$$

or

$$\frac{\partial \phi}{\partial t} + c^2 \nabla_r \cdot \vec V = 0$$

$$\frac{\partial^2 W}{\partial z^2} + \frac{1}{c^2} N^2 W = 0 \qquad (10)$$

where c is the separation constant. On the other hand, operating with $\frac{\partial}{\partial z}$ on the second of (9) and using (10), one can form a

differential equation in G alone:

$$\frac{\partial}{\partial s}\left(\frac{1}{N^2}\frac{\partial G}{\partial s}\right) = -\frac{G}{c^2} \qquad (11).$$

The separation constant c is to be determined by the eigenvalues from the solutions of Eq. (10) or (11) through numerical approximation. The necessary boundary conditions for H and G at $s = 0, 1$ are that $\dot{s} = 0$ (a common choice). Since the vertical motion is defined as

$$wH = \left(\frac{s}{T}\frac{\partial\phi}{\partial t} + \dot{s}\right).$$

This condition implies that H=0 at $s = 0$. Furthermore, using this condition in Eq. (9) at $s = 0$, we have $\frac{\partial G}{\partial s} = 0$ as the other upper boundary condition. At $s = 1$, the situation is slightly more complicated. In addition to $\dot{s} = 0$, the geopotential height at the earth's surface is assumed constant. Thus, at this level we have from (6),

$$G_s = \partial\phi$$

$$H_w = \frac{1}{T}\frac{\partial\phi}{\partial t}$$

and on combination,

$$\frac{\partial\phi}{\partial t} = \partial T H_w \qquad (12).$$

Employing Eq. (9), we arrive at

$$\frac{\partial G}{\partial z} = \frac{-\kappa^2}{RT} G \tag{11}$$

as the lower boundary condition for G. Finally, using (10) and (9) to solve for (11), we find the lower boundary condition for H,

$$\frac{\partial H}{\partial z} = \frac{RT}{c^2} H .$$

For clarification, the vertical system is summarized in Table 1.

Table 1. The vertical problem

Variable	Equation	Boundary Condition: $z = 0$	Boundary Condition: $z = 1$	z-levels
H	$\frac{1}{\eta^2} \frac{\partial^2 H}{\partial z^2} = \frac{[illegible]}{c^2} H$	$H = 0$	$\frac{\partial H}{\partial z} = \frac{R}{c^2} H$	even
G	$\frac{\partial}{\partial z}\left(\frac{1}{\eta^2} \frac{\partial G}{\partial z}\right) = \frac{[illegible]}{c^2} G$	$\frac{\partial G}{\partial z} = 0$	$\frac{\partial G}{\partial z} = \frac{-\kappa^2}{RT} G$	odd

The vertical coordinate (z) is divided into nine equal intervals for numerical purposes. After second order finite differencing is applied, the system, either H or G, takes on the standard eigenproblem form,

$$\underline{M}\,\phi = \lambda\phi \qquad (14)$$

where $\underline{M}$ is a 9×9 coefficient matrix, and $\underline{\phi}$ a 9-element column vector representing the vertical structure function of H or G, and $\lambda = \frac{1}{c^2}$ is the eigenvalue to be determined. The formulation of $\underline{M}$ can be found in Appendix B. It should be noted that H is solved at levels $\sigma_i = \frac{i}{18}$, i even, while G is calculated at i odd, for the parameter Γ^2, which is evaluated using the standard atmosphere, and needs the vertical derivative of specific volume at the surface, which is not available. The resultant eigenvalues from either equation are thus slightly different. Shown in Table 2 are equivalent depths, h_e, converted from the relationship $gh_e = c^2 = \frac{1}{\lambda}$. Figs. 1 and 2 give the eigenstructures of H and G.

Table 2. Equivalent Depths (m)

	H	G
1	9.51091+03	9.55525+03
2	2.41988+03	2.42080+03
3	4.11466+02	4.11181+02
4	9.220[illegible]7+01	9.21716+01
5	5.75777+01	5.75363+01
6	2.12336+01	2.12131+01
7	1.08675+01	1.08581+01
8	6.47477+00	6.46903+00
9	3.990[illegible]0+00	3.98613+00

2.2 Horizontal modes

Separating out the vertical (z) dependence as indicated above, the scalar equations in horizontal coordinates (x,y) and time take the form from (7), where $dx = a\cos\phi\, d\lambda$,

$$\frac{\partial u}{\partial t} \quad - fv + \frac{\partial \phi}{\partial x} = 0$$

$$\frac{\partial v}{\partial t} + fu \quad + \frac{\partial \phi}{\partial y} = 0 \qquad (15)$$

$$\frac{\partial \phi}{\partial t} + c^2 \frac{\partial u}{\partial x} + c^2 \frac{\partial v\cos\phi}{\partial y} = 0$$

or using the periodic expansion as in (8) for longitude, as well as in time (since the equations are linear),

$$\begin{pmatrix} u \\ iv \\ \frac{\phi}{c} \end{pmatrix} = \sum_{m=0}^{\infty} \begin{pmatrix} u_m^*(y) \\ v_m^*(y) \\ \phi_m^*(y) \end{pmatrix} e^{i(m\lambda - \nu t)} \qquad (16)$$

we obtain a form of the standard eigenproblem as

$$(\underset{\sim}{A} - \nu \underset{\sim}{I})\, \overset{\frown}{\gamma} = 0 \qquad (17)$$

where

$$\underset{\sim}{A} = \begin{pmatrix} 0 & f & \frac{mc}{a\cos\phi} \\ f & 0 & \frac{c}{a}\frac{\partial}{\partial \phi} \\ \frac{mc}{a\cos\phi} & \frac{-c}{a\cos\phi}\frac{\partial}{\partial \phi}(\,)\cos\phi & 0 \end{pmatrix}, \qquad \overset{\frown}{\gamma} = \begin{pmatrix} u_m^* \\ v_m^* \\ \phi_m^* \end{pmatrix}.$$

Here, a is the earth's radius, m is the longitudinal wavenumber, σ is the frequency and ψ is the unknown vector. To determine suitable boundary conditions at the poles, we solve Eq. (17) for each unknown and set $\phi = \pm 90°$; the resultant conditions are listed in Table 1.

Table 1. Polar boundary conditions

$m=0$	$m=1$	$m\geq 2$
$u=0$	$u=\pm iv \ (\phi=\pm 90°)$	$u=0$
$v=0$	$v=\pm iu \ (\phi=\pm 90°)$	$v=0$
$\frac{\partial z}{\partial \phi} = 0$	$z=0$	$z=0$

As noted earlier, both a fourth-order finite difference scheme and a second-order finite element method are applied to the system for numerical solution with a grid interval of $\Delta\phi=5°$ latitude. Additional tests with different grid intervals and boundary positions have been made and results will be described. Under discretization, $\bar{\psi}$ becomes a column vector of dimension 105 with the exception of m=0 and 1, because for these two wavenumbers, there are non-zero boundary values to be determined for one of the dependent variables and thus $\bar{\psi}$ has two more degrees of freedom. Correspondingly, $\underset{\sim}{A}$ becomes a matrix of 9 blocks, each having dimension 35x35 for all m other than 0 and 1. The details of these numerical methods may be found in Appendix C.

3. Frequencies, Modes and Structures

Although our primary concern is with the computational modes which arise from the solution to Eqs. (17), we note that the eigensolutions of the system depend on a number of variables. They depend, of course, principally on the dynamics of the model, but also on the boundary conditions, the vertical separation and its numerics, the wave number and the computational scheme. For the latter we select the 4th order difference and finite element schemes for comparison.

Before discussing the general global model we may consider the effects of changing the geometry from pole-to-pole to a channel, and also establish the effect of changing truncation, i.e., varying Δy. For this purpose we have modified our general model to represent a channel from 60°S to 60°N and to include or exclude curvature. Consider now the channel model form utilizing a simple second order finite difference scheme. An example of the effect of changing Δy from 5° lat. to 10° lat. may be seen by Fig. 1. We show on this figure the profile in latitude of the eigenvector for both an external (equivalent depth of 9.5 km) and an internal (equivalent depth of .42 km) mode for wave number one. Both vectors are of the Rossby type with few zeros. Note that there is a distinguishable effect on the external mode by changing the truncation, an effect which is not evident for the internal mode. This indication of an effect, although not conclusive, suggests that care must be taken in choosing a truncation interval and that such a choice may have an impact on the characteristic structures of the model even when those

structures are very smooth.

Next let us consider the effects of the channel approximation, but including curvature effects. Fig. 4 demonstrates the effect of boundaries in a pronounced fashion. We see three examples of boundary modes, modes which are not found in the pole-to-pole model. Demonstrated are latitudinal structures for waves one and six, for both the external and internal vertical profiles of the model. Note how sharply these structures grow near the channel boundary, especially for the internal vertical modes. One must conclude from this demonstration that in a truly nonlinear integration these modes could profoundly influence the ultimate flow evolution with time and yield a flow field substantially different from a pole-to-pole model with similar physical properties.

The effect of changing the position of the boundary on the modal structure of the model may be seen yet more clearly from Fig. 5. Some sample latitudinal structures are displayed for Rossby modes of different wave numbers and for both the external and an internal vertical profiles. Most evident here is the observation that the effect of changing boundaries and/or curvature plays its most predominant role in the longest planetary waves. Thus we can say that boundary effects show up as boundary modes for the channel model with no counterparts in the pole-to-pole case, and that curvature effects have a pronounced impact on modes of the longest planetary waves. Based on these observations, we have chosen to assess the characteristics of a global model with full curvature effects.

The characteristic frequencies which result as a solution to Eq. (13) applied on the sphere will now be demonstrated. We will show first the frequencies for the [illegible] finite difference scheme as discussed in Appendix [illegible]. In Fig. [illegible] we show all the frequencies for both planetary waves [illegible] and [illegible] for the external (first vertical) mode. Note that as indicated [illegible] there are [illegible] such values. The upper branch of the frequency curve is negative (westward propagation) whereas the lower branch is positive (eastward propagation), although the abscissa specifies only amplitude. Fig. [illegible] describes the frequencies for additional planetary waves including waves two, six and ten, also for the first vertical mode.

The most striking character of the frequency distribution is the rapid change (for very low wavenumbers) or the [illegible] (for higher wavenumbers), which occurs on both branches of the curve. This indicates that gravity and Rossby modes can be separated clearly if n is not too small. For very low wavenumbers (e.g. n=1,2) there are a few mixed Rossby-gravity Kelvin waves filling the gap on the descending/ascending branch. For n=0, there are no Rossby mode solutions. As the equivalent depth decreases, frequency tends to decrease, and the separation between gravity and Rossby modes becomes less clear; this is similar to the low wavenumber, external mode result. A demonstration of this observation is seen on Fig. [illegible] which shows the frequencies for all vertical modes and planetary wave [illegible].

The frequencies for the same case (a and b) but using the finite-element truncation are depicted on Fig. [illegible] where

demonstrates the difference in the two computational methods and the frequencies they allow. Note that although the number of eastward and westward gravity modes is the same for the two methods, and that the total number of Rossby modes is also the same, the distribution of Rossby modes is quite different. Whereas there were only 20 westward propagating Rossby modes for the staggered solutions as seen from Fig. 8, there are 24 such modes from the finite element solutions indicated on Fig. 9. Since all the eastward propagating Rossby waves must be computational, the finite element method yields a framework of many more possible physical modes. Whether those modes which fall into the westward propagating group actually are physical modes and will be tested by the procedure to be described in the following section.

5. Computational modes

The eigenfunction solutions to (2.1) have long been known, in general, as a form of Hough functions representing latitudinal structures for given equivalent depth and longitudinal wave number. These modes are often indexed by the number of zero-crossings they have in their structure between the poles. Sometimes the larger index refers to greater structure. It should be noted that the relationship of index and frequency differs between the gravity and Rossby modes. Most apparent, the gravity modes tend to have higher frequency than the Rossby modes, as discussed previously and also noted on Figs. 6, 7, 8 and 9. However, at the separation point between these two modes,

they both have their lower [illegible] for a [illegible] description of this separation would not occur [illegible] on Fig. [illegible]. As frequency increases in magnitude, the index of the gravity modes increases; as the frequency decreases, the index of the Rossby modes increases.

Some of these modes describe physical properties of the model system, whereas some are a consequence of the numerical procedure used to convert the differential equation to numerical form. It is generally established that modes with an index in excess of one-half the number of grid points used in the numerical approximation tend to represent computational modes rather than physical ones. This also suggests that these modes would not represent the original differential equation which was transformed to difference form. Distinguishing computational modes from physical ones is not quite as simple as the preceding might suggest. To exemplify this point, we present the structure of a set of westward propagating gravity modes for the [illegible] component of flow, ordered by frequency. These vectors are for planetary wave six and for the external vertical mode, and their profiles are plotted in Fig. [illegible] based on the [illegible] differencing. Corresponding structures developed for the finite difference method are depicted in Fig. [illegible]. Clearly there is no direct correspondence between frequency and index, and moreover, there is no precise index after which all modes should be defined as computational.

Fortunately a more systematic procedure [illegible] as the "shooting method" is available to make the [illegible] of [illegible]

computational and physical modes more precise. In general, this method attempts to establish whether a frequency and its corresponding vector obtained from the difference system (eq. 27) also satisfies the differential equations from which the difference equations were derived. If the eigenvector and value do not satisfy the differential equations, it is catalogued as a computational mode. The procedure is as follows. Let (27) be written as

[illegible]

[illegible]

[illegible]

On elimination of [illegible], the system is reduced to two equations,

[illegible] (28)

where

[illegible]

The unknown derivatives for u and v can be solved numerically as

an "initial value" problem provided that the parameter σ in the "tendency" matrix and a set of initial data (u_0, v_0) are given. For each individual mode determined as a numerical solution to (17) we insert the eigenfrequency (σ) and the equatorial values of the u- and v-eigenstructures to initialize an integration toward the north pole. If, at the pole, the boundary values of the numerical eigenstructures are not met, σ is adjusted by Newton's method and the integration repeated. More details on this process can be found in Appendix D. The results from this procedure are evaluated to establish the nature of each mode of the difference equations.

Several criteria may be utilized to compare the results of the "shooting" structures with those of the finite-difference equations. We use the following:

a) ratio of frequencies
b) least square difference of structures
c) correlation coefficient between the structures.

The ratio of frequencies may be established once the shooting procedure has converged. This occurs when an adjustment to the frequency derived from the difference system no longer changes the boundary value at the pole to which the shooting procedure integrates, and moreover, this boundary value corresponds to the boundary value applicable to the finite-difference solutions. Alternately, when the boundary values of the two solutions correspond to a preselected small difference, the shooting method

is said to have converged to a "true" physical mode. If, of course, the boundary value is not approached by the shooting method before the frequency changes to one in the vicinity of a different eigenvalue, then we may state that the finite-difference structure in question is indeed a computational mode; i.e., it does not correspond to any mode which satisfies the differential equations. The ratio of frequencies thus measures the converged frequency value of the shooting method to the original frequency with which the method began. Values of this ratio far from unity clearly suggest that the finite-difference system mode either does not approximate the true mode well, or that it represents a computational mode.

In regions of the solution where frequency separation is large, i.e., where sequential frequencies which satisfy the equations change their values substantially, the ratio of frequencies may not be a satisfactory measure to identify a computational mode. Under such conditions it is necessary to have aditional measures and we utilize the comparison of eigenvector structures. Such comparisons are made concurrently with the ratio-of-frequencies, implying that the shooting method, if not converged, has at least been completed. The two procedures identified above as (b) and (c) involve a comparison of the latitudinal structures at all points available from the chosen truncation. Since we use $\Delta\theta = 5°$ latitude, the comparisons are generally made for each physical variable at 35 points. Utilizing these points for both vectors (the original solution and the "shot" solution) we calculate both the least

squares difference and the correlation coefficient. These measures give additional insight into how the two solutions compare. It may happen that the frequencies compare well but the structures do not. Alternately, the frequencies may be different (in those special regions alluded to above) while the structures may be similar. Finally, if the structures have significant amplitude in only a small latitudinal range such as the equatorial region, our statistical measures on structure may still prove to be inadequate to give a definitive answer to the true nature of the difference-equation solution.

To demonstrate the application of the shooting method and the parameters of comparison, we present Table 4. In this table we compare the set of westward propagating gravity waves whose structures (established by solution of (17)) are described on Figs. 10 and 11. We describe solutions for the 4th order difference equations for planetary wave six and for the external vertical mode. Physical as well as computational modes are included in this set (excluding Rossby modes and eastward propagating gravity modes) and indeed without additional criteria, we would consider all of these modes as physical. Let us now determine what the shooting method implies about this set. In the domain of low index values (Figs. 22-35) we see large values of least squares coupled with negligible values of the correlation coefficient. These modes are undoubtedly computational and their structures (Fig. 10) support this conclusion. Note that the ratio-of-frequencies is not a consistently good indicator for selecting computational modes.

Table 4. Statistics on results with the shooting method (Eqs. 16) applied to case for m=6, h_e=9.555 km, 4th order differencing.

No. - number in order of frequency value

Index - number of zero-crossings in structure (*: too high)

f_s - frequency solved from model equations (in $\times 10^{-4}$)

fm - frequency modified by shooting method

L.S. - least square difference of model and shot structures

C.C. - correlation coefficient of model and shot structures

No.	Index	fs	fm	fm/fs	L.S.	C.C.
15	*	7.99	*109.	-11.7	61.6	-0.07
16	11	7.88	8.05	1.02	0.52	-0.41
17	*	7.69	8.05	1.05	0.40	-0.09
18	10	7.59	7.44	0.98	0.41	-0.21
19	*	7.26	7.44	1.02	0.35	-0.00
20	9	7.25	5.76	0.79	0.33	-0.23
21	8	6.87	5.23	0.76	0.23	-0.16
22	*	6.75	6.86	1.02	0.31	-0.08
23	7	6.46	6.86	1.06	0.01	0.95
24	*	6.16	6.30	1.02	0.29	-0.00
25	6	6.03	6.30	1.04	0.01	0.98
26	5	5.59	5.76	1.03	0.00	0.99
27	*	5.51	5.76	1.05	0.25	-0.10
28	4	5.13	5.23	1.02	0.00	1.00
29	*	4.79	5.23	1.09	0.25	-0.00
30	3	4.67	4.73	1.01	0.00	1.00
31	2	4.20	4.23	1.01	0.00	1.00
32	*	4.00	16.8	4.21	0.20	-0.12
33	1	3.73	3.74	1.00	0.00	1.00
34	0	3.24	3.25	1.00	0.00	1.00
35	*	3.13	3.25	1.04	0.05	-0.01

For mode #24 the ratio is only two percent from unity whereas for #32 it is a factor of four. Correspondingly, negligibly small values of least square differences are coupled with unit values of the correlation coefficient, indicating true physical modes. For these modes the ratio-of-frequency is also reasonably close to unity, substantiating our interpretation of their physical nature.

The shooting method has been applied using a 5° increment for integration from equator to pole, a value which corresponds to the increment used to solve the original difference equations. Because we felt that such an increment was too coarse, we tested the process with much smaller intervals, the smallest representing 0.01 degrees of latitude. The results of that experiment were striking. As the increment was decreased from five degrees, the solutions deteriorated, showing the worst results for an increment of one degree. As the increment was further decreased, the results improved gradually. We concluded that the five degree increment for which we gave a demonstration was satisfactory and could not be significantly improved upon.

For the high index modes (Nos. 15-21) our statistics do not indicate any physical modes. However, Fig.10 suggests that some of these modes may by physical. To eliminate this ambiguity, we have modified the shooting method, hopefully to make it more sensitive to high index solutions. Rather than reducing (17) to two first order equations as was done in (18), we reduce the entire set to a single second order equation in one dependent variable, say ψ . This equation may be expressed as follows:

$$\frac{\partial^2\psi}{\partial\phi^2} + p(\phi,\nu)\frac{\partial\psi}{\partial\phi} + r(\phi,\nu)\psi = 0$$

$$p(\phi,\nu) = \frac{2f^2}{\nu^2-f^2}\frac{1}{\tan\phi} - \tan\phi \qquad (19)$$

$$r(\phi,\nu) = \frac{a^2}{c^2}(\nu^2-f^2) - \frac{m^2}{\cos^2\phi} + \frac{mf}{\nu\sin\phi}\left(1 + \frac{2f^2}{\nu^2-f^2}\right) .$$

Utilizing (19) as the shooting equation, two initial values are required. These were chosen as the values of ψ at the equator and at the first point (5° lat). For this modified procedure various increments were also tested, but again such variation had little impact on the solution.

Results for high index modes using this procedure are described in Table 5 which is identical to Table 4 except for the shooting method applied. It is evident by noting the correlation coefficient for modes 16, 18, 20 and 21 that the new technique is considerably more sensitive in this range, and that the correlation coefficient, as well as the other parameters, identifies these modes as physical rather than computational. This effectiveness of system (19) has been tested on other planetary waves and vertical modes with equivalent success, as well as for the finite-element method, the results of which are described on Table 6.

Consequently, we have determined that the appropriate shooting method to use is based on system (19). We have checked carefully to establish that this procedure also successfully

Table 5. Statistics on results with the modified shooting method Eq. (19). All other conditions are the same as for Table 4.

No.	Index	fs	fm	fm/fs	L.S.	C.C.
11	*	8.47	8.37	0.99	0.57	-0.49
12	*	8.46	9.47	1.12	0.51	-0.33
13	*	8.17	8.06	0.99	0.85	-0.47
14	*	8.11	7.64	0.94	0.69	-0.29
15	*	7.99	9.12	1.14	0.83	0.23
16	11	7.88	8.06	1.02	0.22	0.95
17	*	7.69	8.79	1.14	0.75	-0.08
18	10	7.59	7.66	1.01	0.11	0.99
19	*	7.27	7.49	1.03	0.90	-0.03
20	9	7.25	7.27	1.00	0.06	1.00
21	8	6.87	6.85	1.00	0.03	1.00
22	*	6.75	3.72	0.55	0.87	-0.02
23	7	6.46	6.43	1.00	0.01	1.00
24	*	6.16	8.27	1.34	0.87	-0.06
25	6	6.03	6.00	0.99	0.01	1.00

Table 6. Same as Table 5 except for finite-element expansion.

No.	Index	f_s	f_m	f_m/f_s	L.S.	C.C.
11	*	10.00	9.78	0.98	0.05	0.91
12	*	9.99	10.00	1.01	0.21	0.57
13	*	9.78	11.33	1.16	4.01	-0.01
14	*	9.67	9.73	1.01	0.63	0.01
15	*	9.49	11.64	1.23	40.22	-0.02
16	*	9.14	9.47	1.04	0.75	-0.41
17	*	9.12	14.07	1.54	∞	0.32
18	12	8.75	8.44	0.96	0.01	0.99
19	*	8.36	8.27	0.99	0.75	-0.06
20	11	8.34	8.06	0.97	0.01	0.99
21	10	7.91	7.68	0.97	0.00	0.99
22	9	7.46	7.27	0.97	0.00	0.99
23	*	7.40	7.27	0.98	0.33	-0.04
24	8	7.01	6.86	0.98	0.00	1.00
25	7	6.55	6.43	0.98	0.00	1.00
26	*	6.26	6.59	1.05	1.12	-0.06
27	6	6.09	6.00	0.99	0.00	1.00
28	5	5.62	5.56	0.99	0.00	1.00
29	4	5.15	5.11	0.99	0.00	1.00
30	*	4.96	3.72	0.75	0.33	-0.01
31	3	4.68	4.65	1.00	0.00	1.00
32	2	4.20	4.19	1.00	0.00	1.00
33	1	3.73	3.72	1.00	0.00	1.00
34	*	3.50	3.79	1.08	4.98	-0.00
35	0	3.24	3.24	1.00	0.00	1.00

identified the computational modes in the lower index range as was demonstrated for system (18). To definitively identify all possible computational modes we use all three of the parameters specified; (a), (b), and (c). Where possible, we also use the index parameter since when the zero crossings become too frequent (~2Δφ) the solutions are clearly computational. However, such a test is best done visually, and as such is not only subject to human error, but is prohibitively time consuming. Thus we use the correlation coefficient as the prime parameter, noting that unless its value is greater than .95, all indications are that the representative structure is computational. If the condition is met (c.c.>.95), the other two criteria are checked for consistency. In this way we can definitively identify and isolate all computational modes.

Finally, there are a set of modes which cannot exist physically and must be computational; these include all the eastward propagating Rossby modes. They may be identified immediately from their frequency and the shooting method corroborates this identification.

5. Physical vs. Computational Modes

Having established a method whereby the distinction between physical and computational modes characteristic of our model is made evident, we may ask about their relative distributions. This question does not appear to have a unique answer, but some information is available from our calculations, as indicated by Tables 4, 5, and 6. We note that for the external vertical mode, the longest planetary waves have the most physical modes. This relationship is true also for the internal modes, but there is a reduction in the number of physical modes as one proceeds to higher internal modes.

Consider the example of westward propagating gravity modes for the 4th-order difference model. For the external mode, waves zero and one have half physical and half computational modes. As one proceeds to the shorter scales, the ratio of physical to computational modes drops asymptotically to about 20 percent, so that by wave m=13 this minimum ratio has been reached. This minimum ratio seems to apply also for the first three internal modes although the ratio for the longest waves (m=0,1) decreases rapidly, so that for internal mode three (k=4), wave number one has only a 25 percent ratio and drops to 20 percent by wave number nine.

We note further a substantial reduction in physical modes between internal vertical modes four and five, and for yet higher internal modes we see only three physical modes, even at the longest wavelengths. The results clearly indicate that for

highly structured vectors (short waves and internal modes) there are many more computational contributions in the domain of gravity waves.

A similar relationship exists for the Rossby modes, although more physical modes remain for the shorter wavelengths than appear for the gravity modes. We do not have sufficient data to comment on the increase of computational Rossby modes with increasing internal mode, but the correlation does exist. Indeed it is difficult to identify any true physical modes associated with any wavenumbers for the last (ninth) internal mode. Although there is negligible amplitude associated with this mode in atmospheric data, such computational contributions may well infect and deteriorate nonlinear integrations.

It is of interest to note that the physical modes developed from the model equations, at least in the gravity domain, are remarkably similar for the 4th-order and finite-element representations. Perusal of Figs. 10 and 11 make this comparison clear. The computational modes do show some structural differences. This can be seen by comparing the envelopes of computational modes for corresponding vectors on the two figures. If all modes are used in nonlinear integrations, because of the differences in the computational modes, the two systems should yield different results. If, however, the computational modes are filtered from the data and only the physical modes represent the initial conditions, the two systems (4th-order finite difference and finite element) should yield the same integrations until the computational mode amplitudes develop

due to non-linearity.

With reference to the larger number of westward propagating Rossby modes found with the finite-element method, as compared to the finite-difference method, many of these modes proved to be computational. Indeed, for the case of wave number six and the external mode, we note [illegible] physical Rossby modes for the difference system and only [illegible] physical Rossby modes for the finite-element method. Thus our expectation that more westward propagating Rossby modes would lead to more physical modes is not met. Moreover this result indicates how carefully the modal properties of any model must be assessed.

6. Initialization

In the previous section we have highlighted the method whereby computational modes may be separated from physical modes when characteristic solutions of a linearized system are determined. It has also been demonstrated that if a nonlinear model is expanded in these characteristic modes, filtering of the initial data may have a significant impact on the integration properties of the system. In the past such filtering has been imposed on high frequency gravity modes in order to inhibit their propagation in the system. Successes with this procedure suggest that perhaps computational errors due to numerical processes (finite-differencing, etc.) may also be inhibited by filtering initial data of unwanted computational modes.

For complete elimination of computational modes, their initial values as well as higher derivatives in time must be

removed from the initial data. Unfortunately adjusting higher derivatives acts as constraints on the amplitudes of the physical modes which may be unrealistic. We therefore choose only to remove the initial computational modes, reinitializing during integration if those modes grow substantially due to non-linearity. This section will outline the procedure for establishing the contributions of the computational modes in the initial data, how it will be removed, and what its significance in the initial data set is.

To test our procedure, we have chosen a FGGE data set from 00Z, JAN 16, 1979 available from NCAR and prepared and gridded by ECMWF. We utilize for our study a 5° latitude and longitude global grid at the following 12 standard pressure levels given in millibars: 1000, 850, 700, 500, 400, 300, 250, 200, 150, 100, 70, and 50. For our purposes, as will become apparent, we require only the wind component and height fields. The raw data used is that available at 72 equally spaced longitudes, 37 equally spaced latitudes including poles and equator, and at the 12 specified pressure levels.

6.1 Longitudinal Projection

Consistent with our representation of the model in Fourier modes for the longitudinal dependence, as represented by Eq. (16), we transform the original data by a Fourier expansion. Given the data sets for $u(\lambda,\theta,p,t_o)$, $v(\lambda,\theta,p,t_o)$ and $z(\lambda,\theta,p,t_o)$, we calculate the vector $\bar{v}_m$ at each latitude and each pressure level from the transform.

$$\psi_n(p, \phi, t_0) = \frac{1}{2\pi}\int_0^{2\pi} \begin{pmatrix} u(\lambda, \phi, p) \\ v(\lambda, \phi, p) \\ z(\lambda, \phi, p) \end{pmatrix} e^{-in\lambda}\, d\lambda \qquad (20).$$

These integrals must be calculated numerically at all the longitudinal grid points, but since the grid interval is uniform, the numerical integration is identical to the true integral without computational errors. Consistent with the assumptions made previously for the model equations, the data are truncated to include only waves for $n \leq 20$. Since ψ_n is a complex vector, negative wave number contributions may be calculated from the phase angles, if needed.

With this transformation, we now have a data set $\bar{\psi}_n$ which represents twenty waves plus the mean flow at the standard pressure levels and at 37 latitudinal points.

4.2 Vertical projection

To make the data conform in the vertical with the levels chosen for the model, we establish the corresponding pressures which define sigma levels at which the data described by $\bar{\psi}_n$ should be determined. We note from Section 2.1 that all three of the variables described by $\bar{\psi}_n$ are represented by the vectors of $\bar{G}$. From Appendix B it is evident that the σ-levels at which the vectors G are defined are calculated for $\sigma = i/18$, where $1 \leq i \leq 17$ and odd. The pressures at these levels are calculated from the definition of σ (Eq. 2) using $P_t = 10$mb and $P_s = 1000$mb, and are (in millibars), 945, 835, 725, 615, 505, 395, 285, 175, and 65. Using a cubic spline algorithm, the values of the

vectors $\bar{X}_m$ at the standard levels are interpolated to these new levels which correspond to the σ-levels of the model.

Our original data set is now transformed to the Fourier coefficients in longitude applied at 17 equidistant latitudinal points and at nine σ-levels. Since we wish to determine the amplitude of the computational modes (in latitude) from our data set, and since these modes are known from the model for each of the model's vertical modes $\bar{G}$ (through their equivalent depths), we first project our modified data onto those vertical modes.

This process is accomplished as follows. For simplicity consider only one of the variables of the vector $\bar{X}_m$, say u_m. A similar transform can be accomplished for v_m and ϕ_m simply by substituting those variables for u_m in the following discussion. Indeed, an extension of u_m to include the other two variables will allow the process to be completed at once, without repetition. Suppose now that we let u_m be given as a series in the vectors $\bar{G}$. Note that these vectors are described by Fig. 2. Thus,

$$u_m(\theta_i,\sigma_j) = \sum_k u_{m,k}(\theta_i)G_k(\sigma_j) \qquad (21).$$

Here θ_i represent the latitudinal grid points and σ_j represents the nine odd sigma levels. The vectors G_k are those which were derived in Appendix B and described on Fig. 2. The amplitude coefficients $u_{m,k}$ are to be determined. By normalizing and orthogonalyzing the vectors G_k, we may establish the coefficients $u_{m,k}$ by a simple transform:

$$u_{m,k}(\phi_\ell) = \sum_{\substack{j=1\\ \text{odd}}}^{17} u_m(\phi_\ell, \sigma_j) G_k(\sigma_j) \qquad (22).$$

The process is more simply represented by a matrix equation if we define the variables as follows. Let $\underline{u}_m$ be a matrix with elements $u_{m,k}(\phi_\ell)$ of dimension (37x9) and let each of the vertical structures be represented by a vector of nine elements $(G_k(\sigma_j))$ or $\bar{G}_k$. If we now develop a matrix $\underline{G}$ which is made up of all nine of the vectors $\bar{G}_k$, then we have

$$\underset{\sim}{U}_m = \underline{u}_m \underline{G} \qquad (23)$$

where $\underset{\sim}{U}_m$ is a matrix each of whose vectors represents the projection onto the corresponding vector of $\underline{G}$. The latitudinal structures of these vectors correspond to the profiles which are analyzed by our model. We shall denote these vectors $\bar{U}_{m,k}$ where,

$$\underset{\sim}{U}_m = \{\bar{U}_{m,k}\} \qquad (24).$$

It should be evident that there are nine such vectors for each Fourier coefficient m, and that there are in addition an equal number for both the v and ψ fields. By stacking these vectors in the order defined by (20) we may write a matrix of all variables as $\tilde{x}_m$. Note that for each m and each k (vertical mode), the vectors of $\tilde{x}_m$ are created by first setting down all latitudinal point values of u_m, followed by all iv_m and finally by all ψ_m/c. The total length of these vectors is clearly 111, and they may be

labeled $\bar{x}_{m,k}$.

6.3 Latitudinal projection

At this stage of the transformation process, we have our data available for each planetary wave (m) and for each model vertical mode (k) as a vector on the latitudinal grid. To establish the contribution of this latitudinal profile to each of the model modes in latitude, we simply project the data vectors (which we now have) onto those model modes. But those model modes depend on the numerical process used to represent the model, so we must project the data on both the modes of the 4th-order system as well as on those of the finite element system.

These model vectors have been discussed in Section 3 and Appendix C. They are the *eigenvectors of the matrix* $\underset{\sim}{A}$ (see Eq. 17) and may be defined from

$$\underset{\sim}{A} = \underset{\sim}{S}\,\underset{\sim}{\lambda}\,\underset{\sim}{S}^{-1} \qquad (25)$$

where $\underset{\sim}{S}$ is made up of the vectors $\bar{S}_{m,k}$. These vectors are displayed graphically by Fig. 10 for m=6 and k=1 (external mode) based on 4th- order differencing and on Fig. 11 based on finite element analysis. Projection of our data vectors in terms of $\underset{\sim}{S}$ yields,

$$\bar{x}_{m,k} = \underset{\sim}{S}\,\bar{\xi}_{m,k} \qquad (26),$$

and finally, the projection amplitudes are determined by

inversion. Thus we can establish the relative strength of each of the model modes $\bar{\xi}_{m,k}$ in our data sample from,

$$\bar{\xi}_{m,k} = \underset{\sim}{S}^{-1} \bar{x}_{m,k} \qquad (27).$$

It must be recalled that $\underset{\sim}{S}$ depends on the numerical method applied and that we have two separate matrices to consider.

We are now in a position to filter the given observational data of contributions from computational modes. Thus, if the filtered data is utilized in a nonlinear version of the model for which the filtered computational modes are representative, the numerical integration of those filtered initial conditions should show, hopefully, reduced computational effects. Since each of the elements of $\bar{\xi}_{m,k}$ represents the strength of the corresponding vector in the data set, let us first establish how much amplitude of the data is involved in the computational modes. Recall that we have determined in Section 4 how computational modes are to be defined.

To show how these amplitudes distribute amongst the modes, we present Fig. 12 which is representative of wave m=6 and the external vertical mode, k=1. The corresponding structures of the modes are presented on Fig. 10. On Fig. 12 we have connected the physical modes by line segments. For this case of given (m,k), 41 of the 105 modes are physical and the remainder are computational. The amplitude squared ($\xi^2_{m,k}$) of the computational modes when summed accounts for only 8.8% of the total squared amplitude in the data. Since the physical

variables represented are flow and geopotential, we may also equate this squared amplitude to normalized energy. That the physical modes dominate is evident from Fig. 12. This will hopefully be the case with the other scales (m,k). A similar distribution for the finite-element method may be seen from Fig. 13.

We now reconstruct the latitudinal profiles of the data by inverting Eq. (27), however discarding the amplitudes of the computational modes. This is done by using only those values of $\bar{\xi}_{m,k}$ which represent physical modes in making the calculation. Clearly in the example cited, 8.8% of the squared amplitude of the data will be removed. These reconstructed profiles are now in a format to be used as initial conditions for numerical integration with our model. Fig. 14 describes how filtering alters the original profile. The figure describes the latitudinal profiles of $u_{m,k}(\phi)$ both before (dotted) and after (solid for finite difference, dashed for finite element) filtering of computational modes. The integrity of the profile is essentially maintained, but extremes are smoothed. This indicates the impact of the 4th- order finite difference operator as well as the finite-element operator on the profile and how the computational model is able to deal with extreme latitudinal fluctuations which are actually observed. By filtering out unmanageable fluctuations, perhaps these factors will not impose strongly on the nonlinear progression of the solution. The comparable results between the finite-element system and the 4-th order system exist because their physical modes are so similar.

7. Nonlinear integrations

The computational modes identified in the previous sections have their impact during a nonlinear integration of the equations of motion. To assess this impact, we propose to integrate the nonlinear version of our linear system of equations as first presented by Eqs. (1). Our intent is to define the effects of latitudinal space truncation, so we may represent our equations in terms of planetary wave numbers (spectral expansion) and in terms of the model's vertical modes.

Since we have identified the vertical modes, upon which the wind and height fields depend, with the vectors $G_k(\sigma)$, we may expand those variables in terms of the G vectors;

$$\overline{V} = \sum_k \overline{V}_k G_k(\sigma) \tag{28}$$

$$\psi = \sum_k \psi_k G_k(\sigma)$$

where the vectors G_k satisfy the equation,

$$\frac{\partial}{\partial\sigma}\left(\frac{1}{N^2}\frac{\partial G_k}{\partial\sigma}\right) = -\frac{G_k}{c_k{}^2}$$

and

$$\sum_i G_k(\sigma_i)\, G_{k'}(\sigma_i) = \delta_{kk'} \tag{29}$$

The prediction equations as nonlinear forms of (7) may be written as

$$\frac{\partial \overline{V}}{\partial t} + f\vec{k} \times \nabla + \nabla_\sigma \psi = -\nabla \cdot \nabla_\sigma \nabla$$

$$\frac{\partial}{\partial \sigma}\left(\frac{1}{N^2} \frac{\partial^2 \psi}{\partial t \partial \sigma}\right) - \nabla_\sigma \cdot \nabla = -\frac{\partial}{\partial \sigma}\left(\frac{1}{N^2} \nabla \cdot \nabla_\sigma \frac{\partial \psi}{\partial \sigma}\right) \qquad (30).$$

If we neglect vertical advection, (30) represents a set of three nonlinear equations to predict ∇ and ψ. We may now substitute the expansion in vertical modes given by (28) into Eqs. (30). Utilizing the orthogonality of these modes, we will multiply by each mode in turn and sum over all points in the vertical. This yields,

$$\frac{\partial \overline{V}_k}{\partial t} + f\vec{k} \times \overline{V}_k + \nabla_\sigma \psi_k = -\sum_{k',k''} \alpha_{k,k',k''} \overline{V}_{k'} \cdot \nabla \overline{V}_{k''}$$

$$\frac{\partial \psi_k}{\partial t} + c_k^{\,2} \nabla \cdot \overline{V}_k = -\sum_{k',k''} \beta_{k,k',k''} \overline{V}_{k''} \cdot \nabla \psi_{k'} \qquad (31).$$

$$\alpha_{k,k',k''} \equiv \sum_i G_k(\sigma_i) G_{k'}(\sigma_i) G_{k''}(\sigma_i)$$

$$\beta_{k,k',k''} \equiv \sum_i \frac{c_k^{\,2}}{c_{k'}^{\,2}} G_k(\sigma_i) G_{k'}(\sigma_i) G_{k''}(\sigma_i) \equiv \frac{C_k^{\,2}}{C_{k'}^{\,2}} \alpha_{k,k',k''}$$

It is clear from (31) that because of nonlinearity, the vertical modes are interactive and that the amplitude functions $\overline{V}_k$ and ψ_k must be calculated for all k at any time before time extrapolation can continue to the next time level. To simplify the calculation but still maintain the impact of non- linearity on the evolution of the latitudinal computational modes, let us reduce the system to a "shallow-water" one, by simply presuming that only one vertical mode exists in the expansion of (28).

under this constraint the summation on the right hand side of (31) vanishes and the coefficients become,

$$\alpha_k = \beta_k = \sum_i G_k^3(\sigma_i) \qquad (32).$$

Since we shall now consider each vertical mode (k) individually, no loss of generality will be suffered if we drop the "k" subscript. Let us now refer back to Eq. (16) where we have expanded in longitudinal waves denoted by the wave number m. Furthermore we can recall the vector of variables $\overline{\chi}$ as it is defined for each wave (m) and one vertical mode (k). Using the operator matrix, $\underset{\sim}{A}$, and noting the orthogonality of the Fourier functions, system (31) can be rewritten as follows;

$$\frac{\partial \overline{\chi}}{\partial t} + i\underset{\sim}{A}(m,k,\phi)\overline{\chi} = \begin{matrix} q_u \\ q_v \\ q_\psi \end{matrix} \equiv \overline{Q} \qquad (33).$$

This equation applies for each wave (m) and mode (k). The non-linear vector on the right hand side of (33) is defined as follows:

$$q_u \equiv -\alpha_k \int e^{-im\lambda} d\lambda \left[\frac{u}{a\cos\phi}\frac{\partial u}{\partial \lambda} + \frac{v}{a}\frac{\partial u}{\partial \phi} - \frac{uv}{a}\tan\phi\right]$$

$$q_v \equiv -i\alpha_k \int e^{-im\lambda} d\lambda \left[\frac{u}{a\cos\phi}\frac{\partial v}{\partial \lambda} + \frac{v}{a}\frac{\partial v}{\partial \phi} - \frac{u^2\tan\phi}{a}\right] \qquad (34).$$

$$q_\psi \equiv \frac{-\alpha_k}{c_k} \int e^{-im\lambda} d\lambda \left[\frac{u}{a\cos\phi}\frac{\partial \psi}{\partial \lambda} + \frac{v}{a}\frac{\partial \psi}{\partial \phi}\right]$$

It is an easy matter to remove the λ-dependence from the q's by

integration. Because of the nonlinearity, as we expand $\overline{V}$ or ψ in m, the q's will generate a double sum over all wave numbers. However, orthognality requires the simple addition rule to apply. Therefore, the double sums are reduced to single ones over all wave numbers, since we have that m''=m-m'. As an example,

$$-\alpha_k \int e^{-im\lambda} \frac{u}{a\cos\phi} \frac{\partial u}{\partial \lambda} d\lambda = \frac{-2\pi i}{a\cos\phi} \alpha_k \sum_{m'} m' u_{m'} u_{m-m'} \qquad (35).$$

Eq. (35) represents the first member of q_u as described by (34) and shows clearly the nonlinearity. It must be noted that the summation goes over all allowed values of m', here chosen as $|m'|\leq 20$ and that m in (35) refers to the wave number (m) associated with the vector $\overline{\chi}$ in Eq. (33).

Although it is now possible to expand (33) in terms of the latitudinal modal functions developed for the linear problem, we shall simply convert the system by numerical means to a difference system using (a) 4th-order differencing in latitude or (b) finite-element differencing. Both these procedures have been described in detail in Appendix C and need not be reviewed here. However, it should be evident that the left hand side of (35) becomes a matrix set over all latitudinal points and would be satisfied by the normal modes (including computational modes) if nonlinearity did not exist. Thus the vector $\overline{Q}$ must be expanded at all latitudinal grid points and the appropriate difference operator applied. Because of (34) and (35) we see that all grid points and all waves interact to affect any wave at

a particular grid-point.

Given an initial state represented by $\overline{\chi}(t=0)$ for all grid points and planetary waves, as well as for the specified vertical mode, the value of $\overline{\chi}(t)$ can be determined by a suitable time stepping procedure. To accomplish this, we utilized the well tested leapfrog scheme, using a multiple forward start.

At this point the development of initialization as discussed in the previous section comes into play. System (33) in its final form for integration clearly involves computational modes; indeed we have isolated their properties with great care. We have also, however, removed the contributions to these computational modes from the initial data. Thus the integrations should begin without computational modes, but it is clear to see that because of the vector $\overline{Q}$, these modes will be regenerated during the integration. How rapidly this happens and how strongly it depends on the numerical form of the equations will be established by integrating system (33) for both numerical methods with and without the filtering of the computational modes. The growth of the modes can clearly be identified if, during integration, they are monitored. Thus we will be able to establish their impact and the benefit of filtering (initialization). Finally, if growth of the computational modes is rapid, they may be filtered periodically during the integration thereby inhibiting their effect.

Computer programs for the numerical integration of (33) have been prepared and checked, but no successful integrations have yet been run. We cannot therefore report on these experiments,

although we are actively working on this project and hope to complete it soon.

8. Conclusion

In our search to isolate and define computational errors in atmospheric modeling with intent to define the "best" computational schemes, we have uncovered a method which, although not yielding the universally best numerical scheme, will nevertheless provide the needed insight to choose the proper scheme for any particular model. By model we mean here the complete set of model equations including all physics, dynamics, boundary and initial conditions. The procedure is oriented toward space truncation and we have focussed on truncation in the horizontal rather than the vertical. The essence of the technique is to define the normal modes of the linearized version of the model, to expand the initial conditions in terms of these modes, to separate the physical from computational contributions, and to filter the computational modes from the initial data. The model is then integrated with the filtered data and refiltered during integration, as needed.

The primary issues associated with this process are the selection of normal modes for the linear model, the identification of computational modes, and the filtering of the initial data. We have described these procedures in detail by application to a specific model and by using a high quality global data set. The model used is based on the current non-forced GLAS global model using σ-coordinates in the vertical.

The model is linearized on a state of rest and its vertical dependence is transformed to normal modes by converting to a separated difference system using second-order differences. Conventional boundary conditions are applied at the top and bottom of the model. These conditions could have some (although probably not too significant) impact on our conclusions, and more realistic top boundary conditions are discussed in a companion report. The implications of vertical differencing as chosen here also deserve additional study, but again, variations in that procedure may not have a dramatic effect on our findings.

The horizontal equations, as separated from the vertical ones, have themselves been separated into longitudinal and latitudinal modes. Since we are here interested in global prediction, we have used the periodicity properties of the earth's atmosphere in longitude to represent that coordinate by Fourier series, thereby separating out a set of equations in latitude and time for each planetary wave in longitude. This process inhibits computational errors due to differencing in longitude, but aliasing errors may still have an effect in a nonlinear calculation, due to series truncation. The normal modes in latitude may be established once those equations (depending as indicated on both a planetary wave number and a vertical mode) have been converted by some computational approximation to numerical form.

We have used two independent computational methods to transform these equations; a fourth-order finite difference scheme and a finite-element method, both on equal grids of five

degrees latitudes from the north to the south pole. By using two different methods we are able to identify the differences that numerical schemes show when used to integrate complex flow equations. As expected the normal modes that develop from these equations separate into intertia-gravity and Rossby modes. Information from this procedure has been used widely to filter initial data of unwanted frequency (gravity) wave propagation. The separation of the gravity/Rossby modes for the model of our choice shows good comparability with other model mode separation discussed in the literature. The specific issue of our discussion refers to the distinction in this modal set between computational and physical modes.

Computational modes are clearly identifiable under certain conditions, almost impossible to identify under others. One must therefore establish a systematic procedure which will identify them. The technique which we have evolved tests all modes developed from the numerical model to determine if they satisfy the differential equations also. If they do, they are true physical modes: if not, they are computational. Zero crossings of modal structures also give good insight into the distinction between computational and physical modes, but may not be conclusive. Based on three criteria identified and defined in our report, as well as choosing the most successful procedure for testing modes in the differential equations, we believe we can separate the physical from computational modes of a numerical model, and do so definitively.

To show how the computational modes impact on model

integration (forecasting) we have chosen to project a global data set onto all the model modes developed for our test model and calculate the computational contributions. The data set was taken from the FGGE, SOP1, analyzed by ECMWF. Our results show that for at least one wave and vertical mode, 6.0 percent of the mean square amplitude of the data projected onto the computational modes. Although this is not a negligible amplitude, reprojection of the physical mode data (after filtering the computational modes) yielded a profile for the initial data not substantially altered from the nonfiltered profile but with somewhat reduced extremes. This indicates that the filtering process can remove the impact of computational noise without necessarily removing the physical content of the data.

The final step in testing the efficiency of our technique is to integrate the numerical equations with the filtered initial conditions. This procedure will determine how fast computational modes grow during integration and how they impact on the nonlinear evolution of the solution. Moreover, because we have chosen two separate computational schemes, the effect of truncation type on the integration process will become evident. We have outlined the procedure for completing this last step, and we have prepared the programs necessary for its implementation. Unfortunately, these calculations have not yet been completed and we cannot report on their outcome. We are continuing this experiment and will report the results as soon as they are available.

It is our contention that the procedure identified and outlined in this report should prove valuable to the prediction community by reducing the effects of differencing approximations. When our test integrations are completed, we shall apply the procedure to a complex, forced model which is currently operational at GIAS. Finally, although our efforts have focussed on global models, we believe that with some modifications, our scheme can also be applied successfully to limited area models.

Appendix A. The thermodynamic equation

Linearizing but retaining the vertical advection term, the thermodynamic equation (5) becomes

$$\frac{\partial \ell n \Theta}{\partial t} + \sigma \frac{\partial \ell n \Theta}{\partial \sigma} = 0 \qquad \text{(A-1)}.$$

From the Poisson equation,

$$\Theta = T\left(\frac{P_o}{P}\right)^{R/C_p} \qquad (P_o = 1000 \text{ mb})$$

and using the equation of state

$$p\alpha = RT,$$

one has

$$\Theta = p^{C_v/C_p}\,\alpha\,\frac{P_o^{R/C_p}}{R}$$

and thus

$$\frac{\partial \ell n \Theta}{\partial \sigma} = \frac{C_v}{C_p}\frac{1}{\sigma} + \frac{1}{A}\frac{\partial A}{\partial \sigma} \qquad \text{(A-2)}$$

$$\frac{\partial \ell n \Theta}{\partial t} = \frac{C_v}{C_p}\frac{1}{\Pi}\frac{\partial \pi}{\partial t} + \frac{1}{A}\frac{\partial \alpha}{\partial t} \qquad \text{(A-3)}$$

in which perturbation quantities π and α are negligible when compared to quantities of the basic state Π and A,

respectively. Also, from Eq. (6) and the perturbation equation of (4) one obtains

$$\frac{\partial^2 \psi}{\partial t \partial \sigma} = \frac{\partial^2 \phi}{\partial t \partial \sigma} + (A + \sigma \frac{\partial \Lambda}{\partial \sigma}) \frac{\partial \pi}{\partial t}$$

$$\frac{\partial^2 \phi}{\partial t \partial \sigma} = -\Pi \frac{\partial \alpha}{\partial t} - A \frac{\partial \pi}{\partial t} .$$

Adding these two equations yields

$$\frac{\partial \alpha}{\partial t} = \frac{1}{\pi}\left(- \frac{\partial^2 \psi}{\partial t \partial \sigma} + \sigma \frac{\partial \Lambda}{\partial \sigma} \frac{\partial \pi}{\partial t}\right) \qquad \text{(A-4).}$$

Finally, by substituting Eqs. (A-2), (A-3) and (A-4) into (A-1), one gets a thermodynamic equation with the following form,

$$\frac{C_v}{C_p} \frac{1}{\pi} \frac{\partial \pi}{\partial t} - \frac{1}{\Lambda \pi} \left(\frac{\partial^2 \psi}{\partial t \partial \sigma} + \sigma \frac{\partial \Lambda}{\partial \sigma} \frac{\partial \pi}{\partial t}\right) + \frac{C_v}{C_p} \frac{\sigma}{\sigma} + \frac{\sigma}{\Lambda} \frac{\partial \Lambda}{\partial \sigma} = 0$$

or

$$\frac{\partial^2 \psi}{\partial t \partial \sigma} = -N^2 \omega = -B\omega \qquad \text{(A-5)}$$

where

$$N^2 = B = -\Lambda \Pi \left(\frac{C_v}{C_p} \frac{1}{\sigma} + \frac{1}{\Lambda} \frac{\partial \Lambda}{\partial \sigma}\right)$$

and

$$\omega = \sigma + \frac{\sigma}{\pi} \frac{\partial \pi}{\partial t} .$$

Appendix B. Solution of the vertical problem

The second order finite-difference equations for solving H are

$$-\frac{1}{B_2(\Delta\sigma)^2}(-2H_2 + H_4) = \frac{1}{c^2} H_2 \qquad \text{at } \sigma = \frac{2}{18}$$

$$-\frac{1}{B_i(\Delta\sigma)^2}(H_{i-2} - 2H_i + H_{i+2}) = \frac{1}{c^2} H_i \qquad \text{at } \sigma_i = \frac{i}{18}$$

$$i = 4,6,8,\ldots 16$$

$$\frac{1}{2A_{18}\pi\Delta\sigma}(-H_{16} + H_{20}) = \frac{1}{c^2} H_{18} \qquad \text{at } \sigma = 1$$

where $\Delta\sigma = \frac{1}{9}$ and B_i, H_i and A_i are values at $\sigma_i = \frac{i}{18}$, i even. Substituting $H_{20} = 2H_{18} - H_{16}$ into the last equation one has the tri-diagonal coefficient matrix

$$\underline{M} = \frac{1}{(\Delta\sigma)^2}\begin{pmatrix} \frac{2}{B_2} & -\frac{1}{B_2} & 0 \\ -\frac{1}{B_i} & \frac{2}{B_i} & -\frac{1}{B_i} \\ 0 & -\frac{\Delta\sigma}{A_{18}\pi} & \frac{\Delta\sigma}{A_{18}\pi} \end{pmatrix}$$

$$\underline{Z} = \begin{pmatrix} H_2 \\ H_i \\ H_{18} \end{pmatrix}, \quad i = 4,6,8,\ldots 16.$$

To solve for G, the centered finite-difference scheme is applied to the expanded form of Eq. (11);

$$-\frac{1}{B}\left[\frac{\partial^2 G}{\partial\sigma^2} - \left(\frac{\partial}{\partial\sigma}\ell nB\right)\frac{\partial G}{\partial\sigma}\right] = \frac{1}{c^2} G$$

at interior levels. The discretized equations are

$$-\frac{1}{B_2(\Delta\sigma)^2}(-G_1 + G_3) = \frac{G_1}{c^2} \qquad \text{at } \sigma = \frac{1}{18}$$

$$-\frac{1}{B_i}\left[\frac{4}{(\Delta\sigma)^2}(G_{i-2} - 2G_i + G_{i+2}) - \frac{\delta B_i}{\Delta\sigma}(-G_{i-2} + G_{i+2})\right] = \frac{1}{c^2} G_i \qquad \text{at } \sigma = \frac{i}{18}$$

$$-\frac{1}{\Delta\sigma}\left[\frac{1}{B_{16}\Delta\sigma}(G_{15} - G_{17}) - \frac{1}{A_{18}\pi} G_{18}\right] = \frac{1}{c^2} G_{17} \qquad \text{at } \sigma = \frac{17}{18}$$

where $\delta B_i/\Delta\sigma$ is the finite difference form for $\frac{\partial}{\partial\sigma}\ell nB_i$. The first and last of the above three equations were established by evaluating Eq. (11) at $\sigma=1$ and $\sigma=17$ respectively, and incorporating the appropriate boundary conditions at $\sigma=0$ and $\sigma=1$ ($i=18$), the latter given by Eq. (13). For the last equation, $G_{18} = 2G_{17} - G_{16}$ and $G_{16} = (1/2)(G_{17}+G_{15})$ must be used. One has the tri-diagonal coefficient matrix

$$\underline{M} = \frac{-1}{(\Delta\sigma)^2}\begin{pmatrix} -\frac{1}{B_2} & \frac{1}{B_2} & 0 \\ \frac{4+\Delta\sigma\delta B_i}{B_i} & \frac{-8}{B_i} & \frac{4-\Delta\sigma\delta B_i}{B_i} \\ 0 & \frac{1}{B_{16}} + \frac{\Delta\sigma}{2A_{18}\pi} & \frac{1}{B_{16}} - \frac{3\Delta\sigma}{2A_{18}\pi} \end{pmatrix}$$

$$\underline{Z} = \begin{pmatrix} G_1 \\ \vdots \\ G_i \\ \vdots \\ G_{17} \end{pmatrix} \qquad i = 3,5,7,\ldots 15.$$

Appendix C. Solution of the horizontal modes

The horizontal modes for given equivalent depth (denoted c) and for specified longitudinal wavenumber (m) are determined from Eq. (17) which is given as

$$(\underset{\sim}{A}-\nu\underset{\sim}{I})\overline{\chi} = 0 \ ,$$

$$\underset{\sim}{A} = \begin{pmatrix} 0 & f & \dfrac{mc}{a\cos\phi} \\ f & 0 & \dfrac{c}{a}\dfrac{\partial}{\partial\phi} \\ \dfrac{mc}{a\cos\phi} & \dfrac{-c}{a\cos\phi}\,\dfrac{\partial\ (\ )\cos\phi}{\partial\phi} & 0 \end{pmatrix} \quad \text{and} \quad \overline{\chi} = \begin{pmatrix} u \\ v \\ \psi \end{pmatrix}$$

where we suppress the subscript m on the vector elements of $\overline{\chi}$. After discretization, the vector $\overline{\chi}$ of unknowns consists of 111 elements for a 5° latitude increment including polar values. Each element in $\underset{\sim}{A}$ forms a square block of size 37. Moreover, non-derivative blocks are diagonal. Using the 4th-order finite differencing scheme given as

$$\left(\frac{\partial x}{\partial y}\right)_j = \frac{4}{3}\left(\frac{x_{j+1}-x_{j-1}}{2\Delta y}\right) - \frac{1}{3}\left(\frac{x_{j+2}-x_{j-2}}{4\Delta y}\right)$$

$$= -\frac{1}{12\Delta y}\,x_{j+2} + \frac{2}{3\Delta y}\,x_{j+1} - \frac{2}{3\Delta y}\,x_{j-1} + \frac{1}{12\Delta y}\,x_{j-2}$$

a band coefficient matrix with width 5 (zero diagonal except the two corners) is formed for a derivative block. More specificially, and to see how the boundary conditions are applied to the numerical scheme, let us write down the basic finite difference formula at any latitude other than the pole; e.g., 85°N:

$$\frac{\partial\psi}{\partial y})_{85} = -\gamma(\psi_{95} - 8\psi_{90} + 8\psi_{80} - \psi_{75})$$

where $\gamma = \frac{1}{12\Delta y}$, $\frac{\Delta y}{a} = 5^0$ and subscripts indicate degrees of latitude, northern hemisphere. For those grid point values at latitudes greater than 90°, one must use the following expression which is always true and is thus unlike the given boundary conditions which only hold at the poles. If λ and y represent longitude and latitude, respectively, one can show that

$$v(\lambda,y) = -(-1)^m v(\lambda+\pi,\ y)$$

$$\psi(\lambda,y) = (-1)^m \psi(\lambda+\pi,\ y)$$

by referring to the Fourier expansion given in Eq. (16) and using

$$e^{im(\lambda+\pi)} = (-1)^m e^{im\lambda} \ .$$

A negative sign is needed in the v-formula because the reference frame changes direction across the pole. For example,

$$v_{95} = -(-1)^m v_{85}$$

$$\psi_{95} = (-1)^m \psi_{85}.$$

Owing to the differences of boundary conditions, there are three cases to consider. Discussion is focused on the northpole. The situation at the southpole is similar.

Case 1. $m>2$: all three unknowns vanish at the pole.

Finite differencing is needed only between 85°N and 85°S. Beginning from the northernmost point the first three grid points yield

$$
\begin{aligned}
\left.\frac{\partial\psi}{\partial y}\right)_{85} &= \gamma(-\psi_{95}+8\psi_{90} \qquad -8\psi_{80}+\psi_{75}) \\
&= \gamma(\qquad \pm\psi_{85}-8\psi_{80}+\psi_{75}) \qquad +/-\text{: if } m \text{ odd/even}
\end{aligned}
$$

$$
\begin{aligned}
\left.\frac{\partial\psi}{\partial y}\right)_{80} &= \gamma(\qquad -\psi_{90}+8\psi_{85} \qquad -8\psi_{75}+\psi_{70}) \\
&= \gamma(\qquad +8\psi_{85} \qquad -8\psi_{75}+\psi_{70}) \\
\left.\frac{\partial\psi}{\partial y}\right)_{75} &= \gamma(\qquad -\psi_{85}+8\psi_{80} \; -8\psi_{70}+\psi_{65}).
\end{aligned}
$$

Hence, the upper left corner of the $\frac{c}{a}\frac{\partial\psi}{\partial\phi}$ block has the form

$$
\frac{c}{a}\gamma \begin{pmatrix} \pm1 & -8 & 1 & & & \\ 8 & 0 & -8 & 1 & & \\ -1 & 8 & 0 & -8 & 1 & \\ & \ddots & \ddots & \ddots & \ddots & \ddots \end{pmatrix} \begin{pmatrix} \psi_{85} \\ \psi_{80} \\ \psi_{75} \\ \vdots \end{pmatrix} = \frac{c\gamma}{a}\,\underset{\sim}{W}\bar{\psi}, \qquad \text{(C-1)}
$$

the band coefficient matrix alluded to earlier. For the other derivative term, one has, noting that $y=a\phi$,

$$\left[\frac{1}{\cos\phi}\frac{\partial}{\partial\phi}(v\cos\phi)\right]_{85} = \frac{\gamma}{\cos\phi_{85}}(-v_{95}\cos\phi_{95}+8v_{90}\cos\phi_{90}-8v_{80}\cos\phi_{80}+v_{75}\cos\phi_{75})$$

$$= \gamma\left(\pm v_{85}-8v_{80}\frac{\cos\phi_{80}}{\cos\phi_{85}}+v_{75}\frac{\cos\phi_{75}}{\cos\phi_{85}}\right)$$

$$\left[\frac{1}{\cos\phi}\frac{\partial}{\partial\phi}(v\cos\phi)\right]_{80} = \frac{\gamma}{\cos\phi_{80}}(-v_{90}\cos\phi_{90}+8v_{85}\cos\phi_{85}-8v_{75}\cos\phi_{75}+v_{70}\cos\phi_{70})$$

$$= \gamma\left(8v_{85}\frac{\cos\phi_{85}}{\cos\phi_{80}}-8v_{75}\frac{\cos\phi_{75}}{\cos\phi_{80}}+v_{70}\frac{\cos\phi_{70}}{\cos\phi_{80}}\right).$$

Except for ratios of cosines, these equations give the same coefficient matrix as $\underset{\sim}{W}$.

Case 2. m=0: ψ does not vanish at the pole.

For the first derivative term one has,

$$\left.\frac{\partial\psi}{\partial y}\right)_{85} = \gamma(-\psi_{95}+8\psi_{90}-8\psi_{80}+\psi_{75})$$

$$= \gamma(8\psi_{90}-\psi_{85}-8\psi_{80}+\psi_{75})$$

$$\left.\frac{\partial\psi}{\partial y}\right)_{80} = \gamma(-\psi_{90}+8\psi_{85}-8\psi_{75}+\psi_{70}).$$

It is seen that there will be an extra column for coefficients of ψ_{90} added to $\underset{\sim}{W}$ of Eq. (C-1), expanding its dimension to 35x37. For the other derivative term, finite differencing at the pole is needed. To achieve this, we write

$$\frac{1}{\cos\phi}\frac{\partial}{\partial\phi}(v\cos\phi) = \frac{\partial(v\cos\phi)}{\partial(\sin\phi)} = \frac{\partial p}{\partial z},$$

treating $z=\sin\phi$ as the independent variable and $p=v\cos\phi$ as the dependent one. Using a second order Taylor's expansion

$$P_{85} = P_{90}+\frac{\partial P}{\partial Z})_{90}(Z_{85}-Z_{90})+\frac{\partial^2 P}{\partial Z^2})_{90}\ \frac{(Z_{85}-Z_{90})^2}{2}$$

$$P_{80} = P_{90}+\frac{\partial P}{\partial Z})_{90}(Z_{80}-Z_{90})+\frac{\partial^2 P}{\partial Z^2})_{90}\ \frac{(Z_{80}-Z_{90})^2}{2},$$

and eliminating $\frac{\partial^2 P}{\partial Z^2})_{90}$, one can solve for $\frac{\partial P}{\partial Z})_{90}$:

$$\frac{\partial P}{\partial Z})_{90} = -(\frac{1-\sin\phi_{80}}{\sin\phi_{85}-\sin\phi_{80}}\ \frac{\cos\phi_{85}}{1-\sin\phi_{85}})v_{85}-(\frac{1-\sin\phi_{85}}{\sin\phi_{80}-\sin\phi_{85}}\ \frac{\cos\phi_{80}}{1-\sin\phi_{80}})v_{80}.$$

Hence, there will be an extra row for coefficients of v_{85} and v_{80} added to the corresponding block of case 1, expanding its dimension to 37x35. The characteristics of the completed coefficient matrix is sketched below.

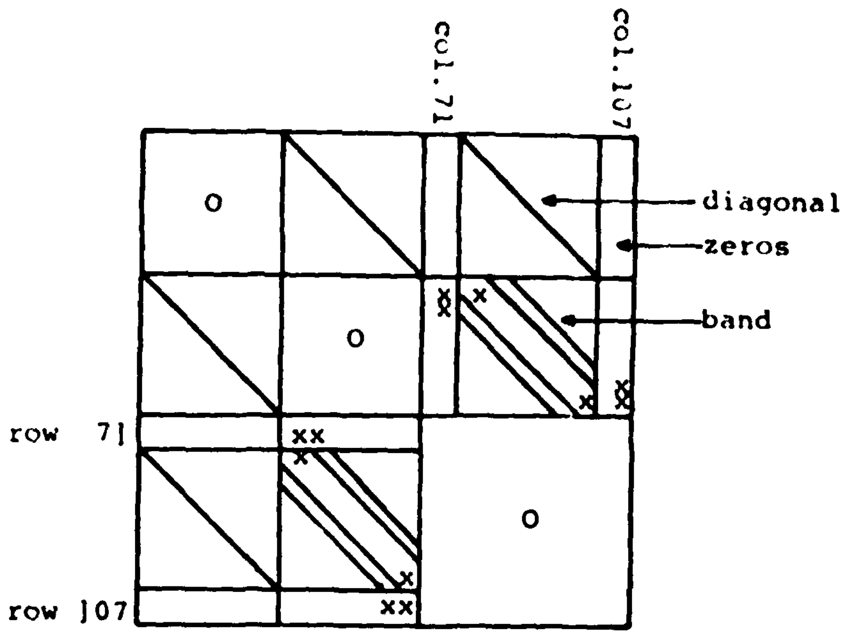

<u>Case 3.</u> m=1: only ψ vanishes at the pole.

One needs a finite-difference form for $\frac{\partial\psi}{\partial\phi}$ at the pole. We choose a one-sided, 4th-order scheme

$$\left.\frac{\partial\psi}{\partial\phi}\right)_{90} = \frac{4}{3}\,\frac{\psi_{90}-\psi_{85}}{\Delta\phi} - \frac{1}{3}\,\frac{\psi_{90}-\psi_{80}}{2\Delta\phi}$$

$$= \gamma(-16\psi_{85}+2\psi_{80}).$$

The other derivative term is first expanded before being approximated by finite differencing:

$$\left[\frac{1}{\cos\phi}\,\frac{\partial}{\partial\phi}\,(v\cos\phi)\right]_{85} = \left[\frac{\partial v}{\partial\phi} - v\tan\phi\right]_{85}$$

$$= \gamma(-v_{95}+8v_{90}-8v_{80}+v_{75})-v_{85}\tan\phi_{85}$$

$$= 8\gamma v_{90}-(\gamma+\tan\phi_{85})v_{85}-8\gamma v_{80}+\gamma v_{75}$$

The remaining discretized equations are identical to those in

case 1.

In this case, there is a non-zero coefficient of u_{96} from the Coriolis term and one must use the boundary condition u=-v at the pole to shift this coefficient to v_{96}. Thus the polar values of u need not be defined. Two corresponding columns and rows are therefore removed. The complete structure of this coefficient matrix is given below.

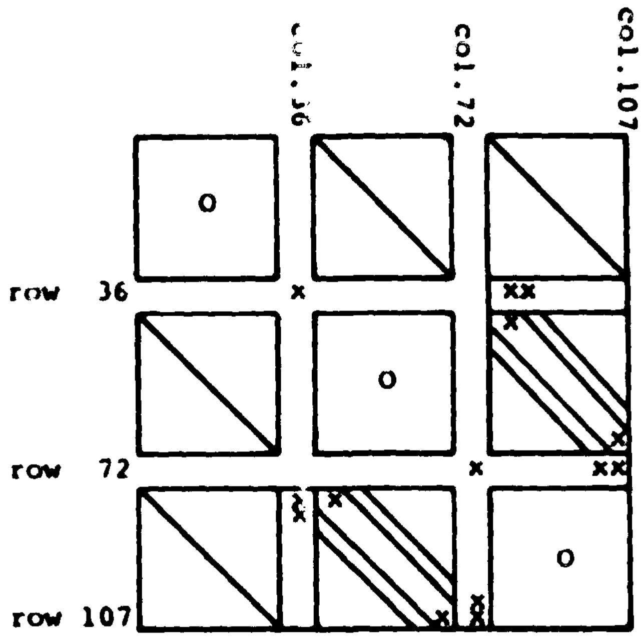

For the finite-element method, each dependent variable is expanded in a set of linear space functions, B(φ),

$$\begin{pmatrix} u(\phi) \\ v(\phi) \\ \Phi(\phi) \end{pmatrix} = \sum_{j=1}^{N} \begin{pmatrix} u_j \\ v_j \\ \Phi_j \end{pmatrix} B_j(\phi) \qquad (C.2)$$

where $B_j(\phi)$ are basic functions for splines of first degree defined as

$$B_j(\phi) = \begin{cases} 0 & \phi < \phi_{j-1} \\ \dfrac{\phi-\phi_{j-1}}{\phi_j-\phi_{j-1}} & \phi_{j-1} \le \phi \le \phi_j \\ \dfrac{\phi-\phi_{j+1}}{\phi_{j+1}-\phi_j} & \phi_j \le \phi \le \phi_{j+1} \\ 0 & \phi_{j+1} < \phi . \end{cases}$$

Note that we again drop the m subscript on elements of the vector $\tilde{\Phi}$. Substituting Eq. (C.2) into Eq. (17) and multiplying by $a\cos\phi$, the system yields

$$-a\nu\cos\phi \sum_{j=1}^{N} u_j B_j + a\Omega\sin2\phi \sum v_j B_j + mc \sum \Phi_j B_j = 0$$

$$-a\nu\cos\phi \sum v_j B_j + a\Omega\sin2\phi \sum u_j B_j + c\cos\phi \sum \Phi_j \frac{\partial B_j}{\partial\phi} = 0$$

$$-a\nu\cos\phi \sum \Phi_j B_j + mc \sum u_j B_j - c \sum v_j \frac{\partial}{\partial\phi}(B_j\cos\phi) = 0 .$$

For the case when all boundary values are zero, the discretized system becomes

$$-\nu\begin{pmatrix} S & 0 & 0 \\ 0 & S & 0 \\ 0 & 0 & S \end{pmatrix}\begin{pmatrix} \vec{u} \\ \vec{v} \\ \vec{\gamma} \end{pmatrix} + \begin{pmatrix} 0 & F & T \\ F & 0 & W \\ T & \tilde{W} & 0 \end{pmatrix}\begin{pmatrix} \vec{u} \\ \vec{v} \\ \vec{\gamma} \end{pmatrix} = 0 \qquad \text{(C.3)}$$

where $\vec{u} = (u_N, u_{N-1}, \ldots, u_j, \ldots, u_2, u_1)^T$, and similarly for $\vec{v}$ and $\vec{\gamma}$. The blocks of the coefficient matrix are to be constructed as follows. One multiplies each term by $B_k(\phi)$ and integrates over the domain. For instance, from the first term one gets,

$$\int_{-\pi/2}^{\pi/2} -a\nu\cos\phi B_k(\phi)\sum_{j=1}^{N} u_j B_j(\phi)d\phi = -\nu\sum_{j=k-1}^{k+1} s_{kj}u_j$$

where

$$s_{kj} = \int_{\phi_{k-1}}^{\phi_{k+1}} a\cos\phi B_k B_j d\phi$$

is the element of S at the k^{th} row and j^{th} column. Notice that $B_k B_j = 0$ if $|k-j|>1$. Similarly,

$$f_{kj} = \int_{\phi_{k-1}}^{\phi_{k+1}} a\Omega\sin 2\phi B_k B_j d\phi$$

$$t_{kj} = \int_{\phi_{k-1}}^{\phi_{k+1}} \sigma c B_k B_j d\phi$$

$$\tilde{w}_{kj} = \int_{\phi_{k-1}}^{\phi_{k+1}} c\cos\phi B_k \frac{\partial B_j}{\partial\phi} d\phi \ .$$

It must be pointed out that

$$\tilde{w}_{kj} = \int_{\pi/2}^{\pi/2} -cB_k \frac{\partial}{\partial\phi}(B_j\cos\phi)d\phi$$

$$= -cB_kB_j\cos\phi \Big|_{-\pi/2}^{\pi/2} + \int_{-\pi/2}^{\pi/2} cB_j\cos\phi \frac{\partial B_k}{\partial\phi} d\phi$$

$$= \int_{\phi_{k-1}}^{\phi_{k+1}} c\cos\phi B_j \frac{\partial B_k}{\partial\phi} d\phi = w_{jk}.$$

This shows that matrices W and $\tilde{W}$ are the transpose of one another. Once again, all blocks are square and tridiagonal with dimensions of 35 provided that all variables vanish at the pole. Furthermore, Eq. (C.3) can be put in the following standard form:

$$(\underset{\sim}{A}-\nu\underset{\sim}{I})\bar{x} = 0 \qquad \text{(C-4)}$$

$$\underset{\sim}{A} = \begin{pmatrix} 0 & S^{-1}F & S^{-1}T \\ S^{-1}F & 0 & S^{-1}W \\ S^{-1}T & S^{-1}\tilde{W} & 0 \end{pmatrix}$$

and S^{-1} is the inverse matrix of S.

For the case of m=0, ψ does not vanish at the poles. The bottom-right S-block of (C.3) is consequently expanded to 37x37, W to 35x37 and $\tilde{W}$ to 37x35. One still obtains a standard eigenproblem. In the case of m=1, u and v have non-zero boundary values. The $\underset{\sim}{A}$ matrix is thereby expanded to $(37+37+35)^2$, and the

details of (C.4) look as follows:

$$\nu \begin{pmatrix} I_{37\times 37} & 0 & 0 \\ 0 & I_{37\times 37} & 0 \\ 0 & 0 & I_{35\times 35} \end{pmatrix} \begin{pmatrix} u_{37} \\ v_{37} \\ \psi_{35} \end{pmatrix} =$$

$$= \begin{pmatrix} 0 & S^{-1}_{37\times 37}\ F_{37\times 37} & S^{-1}_{37\times 37}\ T_{37\times 35} \\ S^{-1}_{37\times 37}\ F_{37\times 37} & 0 & S^{-1}_{37\times 37}\ W_{37\times 35} \\ S^{-1}_{35\times 35}\ T_{35\times 37} & S^{1}_{35\times 35}\ \tilde{W}_{35\times 37} & 0 \end{pmatrix} \begin{pmatrix} u_{37} \\ v_{37} \\ \psi_{35} \end{pmatrix} .$$

Finally, using the boundary conditions of $u_1 = -v_1$ and $u_{37} = v_{37}$, one can shift column 1 and 37 to 38 and 74, respectively, then remove columns and rows of 1 and 37. The resulting system has dimensions of 107.

Appendix D. The Shooting Method

Rewrite the differential equations (18) in matrix form as

$$\frac{\partial}{\partial y}\,\bar{v} = \underline{E}\,\bar{v}$$

and approximate by an implicit finite-difference scheme such that

$$\frac{\bar{v}_{j+1} - \bar{v}_j}{\Delta y} = \underline{E}_{j+1/2}\;\frac{\bar{v}_{j+1} + \bar{v}_j}{2}$$

or

$$\bar{v}_{j+1} = (\underline{I} - \frac{\Delta y}{2}\,\underline{E}_{j+1/2})^{-1}(\underline{I} + \frac{\Delta y}{2}\,\underline{E}_{j+1/2})\bar{v}_j \qquad \text{(D.1)}$$

$$= \underline{F}(y_{j+1/2};\nu)\bar{v}_j$$

where $\bar{v}_j = [u(y_j),\ v(y_j)]^T$ and $\underline{F}$ is a 2x2 matrix with elements functionally dependent on $y_{j+1/2}$ and ν . In addition, the rate of change of $\bar{v}_j$ with respect to ν at each grid point is computed from

$$(\frac{\partial\bar{v}}{\partial\nu})_{j+1} = \frac{\partial\underline{F}}{\partial\nu}\,\bar{v}_j + \underline{F}(\frac{\partial\bar{v}}{\partial\nu})_j \qquad \text{(D.2)}.$$

At the end of the integration $(y=y_J)$, $\bar{v}_J$ can be forced to converge to $\bar{v}_B$ (the value specified by the boundary condition) by a modified frequency, ν_m, according to Newton's method. Using a numerical approach,

$$\left(\frac{\partial \bar{v}}{\partial \nu}\right)_J = \frac{\bar{v}_B - \bar{v}_J}{\nu_m - \nu} \qquad \text{(D-3).}$$

ν_m may be calculated from (D-3) and the derivative may be calculated from (D-2). Since we only need the boundary value (point J), (D-2) is integrated along with $\bar{v}_j$ noting only that $\frac{\partial \bar{v}}{\partial \nu})_{j=0}$ vanishes because of the fixed boundary (initial) value. To cycle the shooting method, the new value (ν_m) is used in (D-1).

References

Baer, F., 1977: Adjustments of initial conditions required to suppress gravity oscillations in non-linear flows. Beitrage zur Physik der Atmosphare, 50, 350-366.

Daley, R., 1980: On the optimal specification of the initial state for deterministic forecasting. Mon. Wea. Rev., 108, 1719-1735.

Dickinson, R.E., and D. L. Williamson, 1972: Free oscillations of a discrete statified fluid with application to numerical weather prediction. J. Atmos. Sci., 29, 623-640.

Gadd, A. J., 1978: A split explicit integration scheme for numerical weather prediction. Quart. J. R. Met. Soc., 104, 569-582.

Machenhauer, B., 1977: On the dynamics of gravity oscillations in a shallow water mode, with applications to non-linear normal mode initialization. Beitrage zur Physik der Atmosphare, 50, 253-271.

Somerville, R. C. J., et al., 1974: The GISS model of the global atmosphere. J. Atmos. Sci., 31, 84-117.

Staniforth, A. and R. Daley, 1977: A finite-element formulation for the vertical discretization of sigma coordinate primitive equation model. Mon. Wea. Rev., 105, 1108-1118.

Williamson, D. L., 1976a: Linear stability of finite-difference approximations on a uniform latitude-longitude grid with Fourier filtering. Mon. Wea. Rev., 104, 31-41.

__________, 1976b: Normal mode initialization procedure applied to forecasts with the global shallow water equations. Mon. Wea. Rev., 104, 195-206.

__________, and R. E. Dickinson, 1976: Free oscillation of the NCAR global circulation model. Mon. Wea. Rev., 104, 1372-1391.

Figure Captions

Fig. 1 Vertical structures of the vertical motion field. There are 9 eigenvectors solved from the H-equation (Eq. 10), ordered by decreasing equivalent depth (left to right, top to bottom). The top (ordinate level 1) is at $\sigma = \frac{1}{9}$ and the bottom $\sigma = 1$. All unmarked abscissas range between ± 1.

Fig. 2 Vertical structures of the wind and height fields. There are 9 eigenvectors solved from the G-equation (Eq. 11), ordered by decreasing equivalent depth. Level 1 is at $\sigma = \frac{1}{18}$ level 9 at $\frac{17}{18}$, , and interior levels are at $\frac{2j+1}{18}$.

Fig. 3 Comparison of modes for 5° and 10° latitudinal increment.

Fig. 4 Boundary modes for channel model between 60°N and 60°S.

Fig. 5 Low-order Rossby modes as they depend on model geometry.

Fig. 6 Eigenfrequencies for longitudinal wavenumbers m = 0 and 1 with equivalent depth 9.555 km (external modes). The abscissa is the order of magnitude of frequency in sec^{-1}. The ordinate is the order of frequencies from the most negative (#1) to the most positive (#107).

First and last 35 frequencies represent westward and eastward gravity modes, respectively. The last mode with negative frequency is #58. There are no values in the range of Rossby modes from #36 to #72 for m = 0. Elsewhere, if neighboring values are too close, only one of them is plotted.

Fig. 7 Same as Fig. 6 except for m = 2, 6, 10. Zero's are used for m = 10.

Fig. 8 Same as Fig. 6 except for m=6. Frequencies for all 9 equivalent depths are plotted (finite difference).

Fig. 9 Same as Fig. 8 except that the finite element method is used to establish the eigenproblem. Notice that there are more negative and relatively less positive Rossby modes than for the finite difference result.

Fig. 10 Latitudinal eigenstructures of u for m = 6 and equivalent depth 9.555 km. Shown are westward gravity modes from #21 to #35, each plotted from pole-to-pole at a 5° increment. Whether a mode is computational or physical is denoted by a c or a p and they are sequenced.

Fig. 11 Same as Fig. 10 except for results from the finite element method.

Fig. 12 Amplitudes of real data set projections onto the

latitudinal modes of the 4-th order difference model for $m = 6$ and equivalent depth 9.555 km. The abscissa represents order of magnitude of amplitude and the ordinate gives order number of modes. Physical modes are indicated by connecting segments.

Fig. 13 Same as Fig. 12 except for the finite-elemen odel modes.

Fig. 14 Comparison of original and reconstructed latitudinal profiles. Dotted line is the real part of observed u after projecting onto the first (external) vertical mode for $m=6$. Solid line is the reconstructed profile by removing amplitudes of computational modes using the finite difference method for normal mode analysis. Broken line is the reconstructed profile based on filtering with the finite element modes.

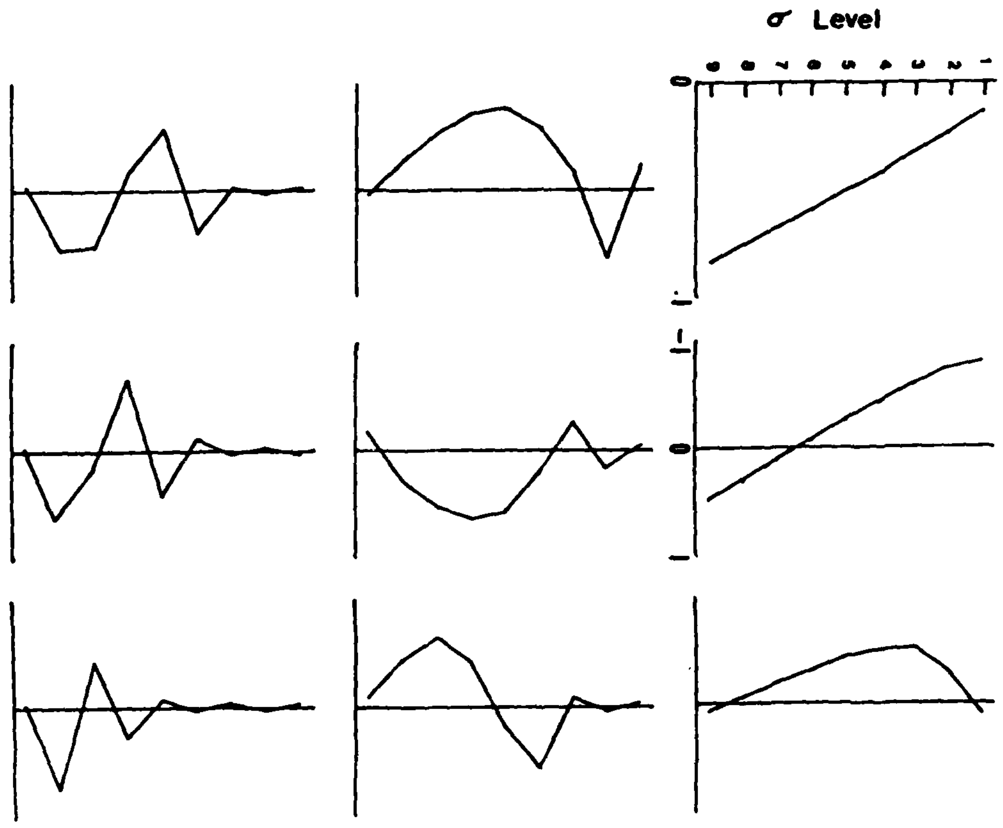

Fig. 1 Vertical structures of the vertical motion field. There are 9 eigen-vectors solved from the H-equation (Eq.10), ordered by decreasing equivalent depth (left to right, top to bottom). The top (ordinate level 1) is at $\sigma = \frac{1}{9}$ and the bottom $\sigma = 1$. All unmarked abscissas range between ± 1.

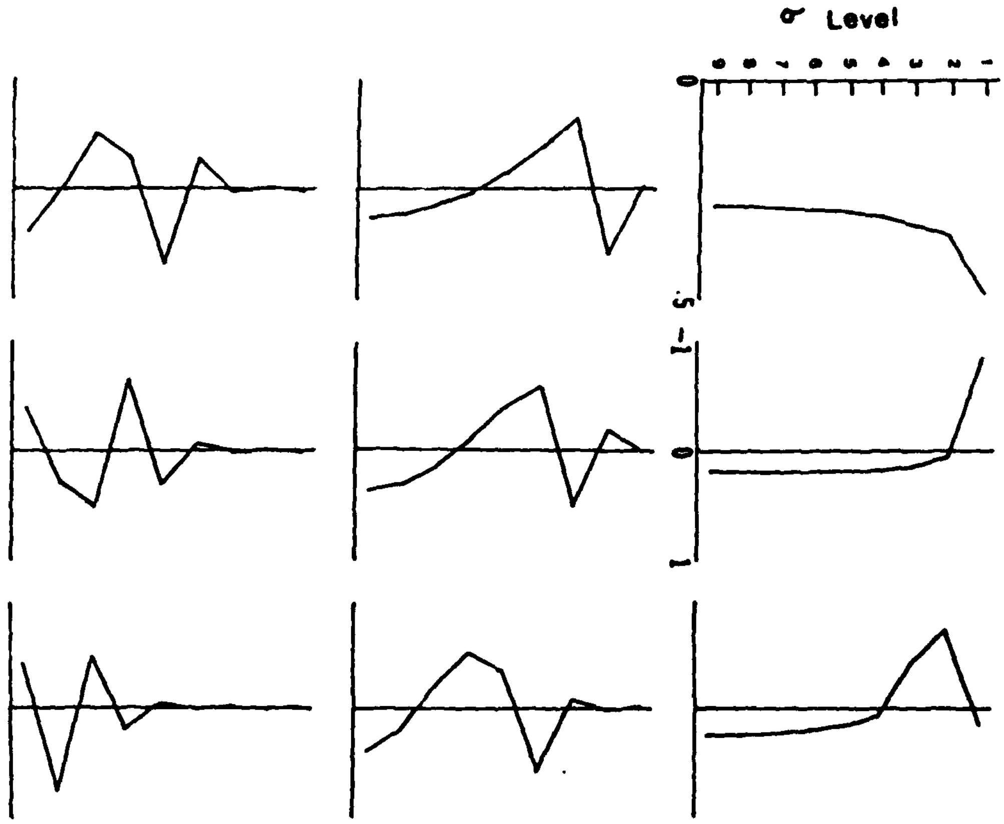

Fig. 2 Vertical structures of the wind and height fields. There are 9 eigenvectors solved from the G-equation (Eq. 11), ordered by decreasing equivalent depth. Level 1 is at $\sigma = \frac{1}{18}$ level 9 at $\frac{17}{18}$, and interior levels are at $\frac{2j+1}{18}$.

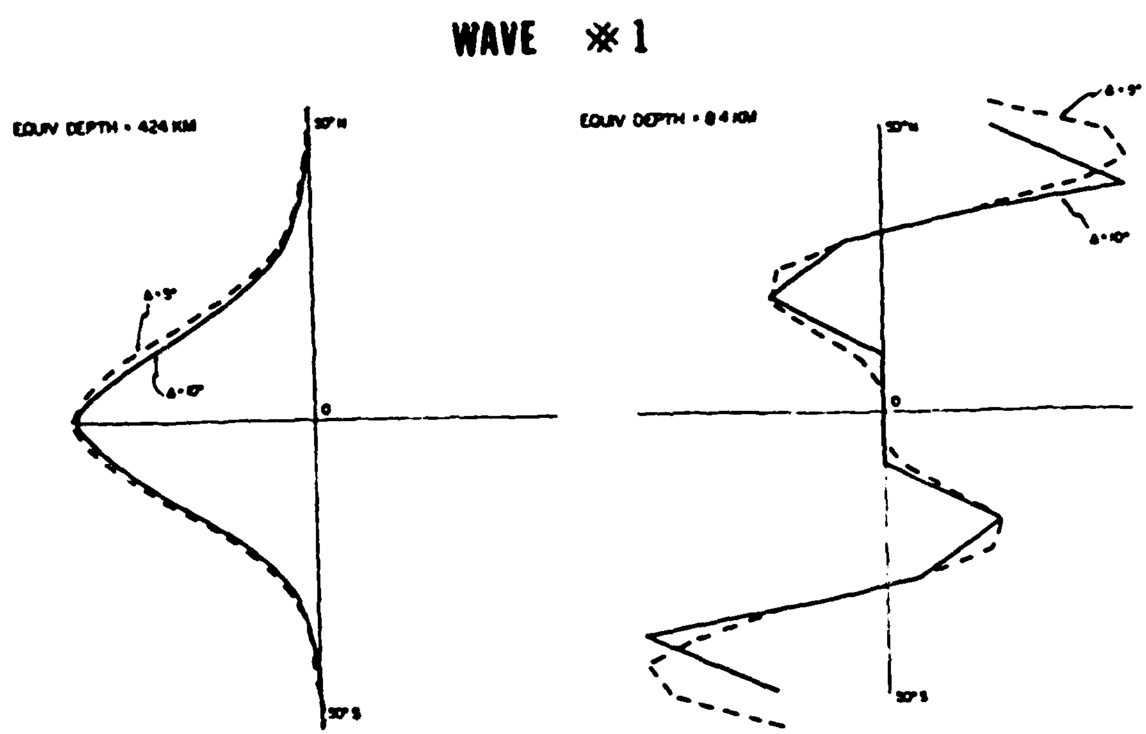

Fig. 3 Comparison of modes for 5° and 10° latitudinal increment.

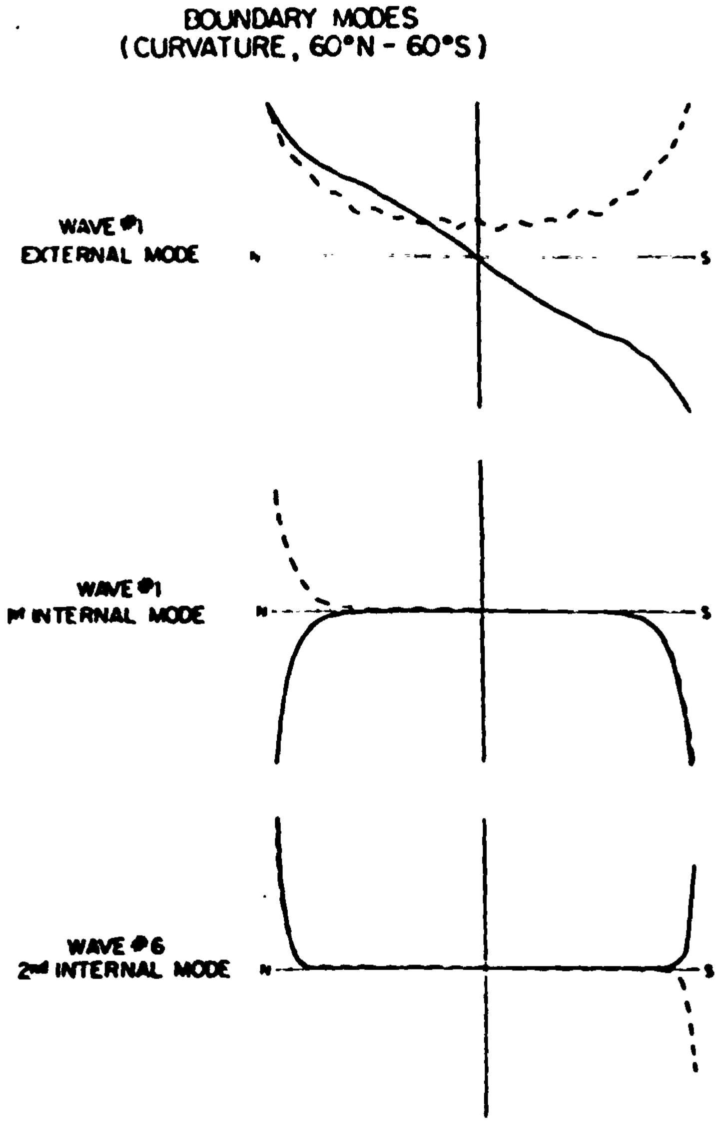

Fig. 4 Boundary modes for channel model between 60°N and 60°S.

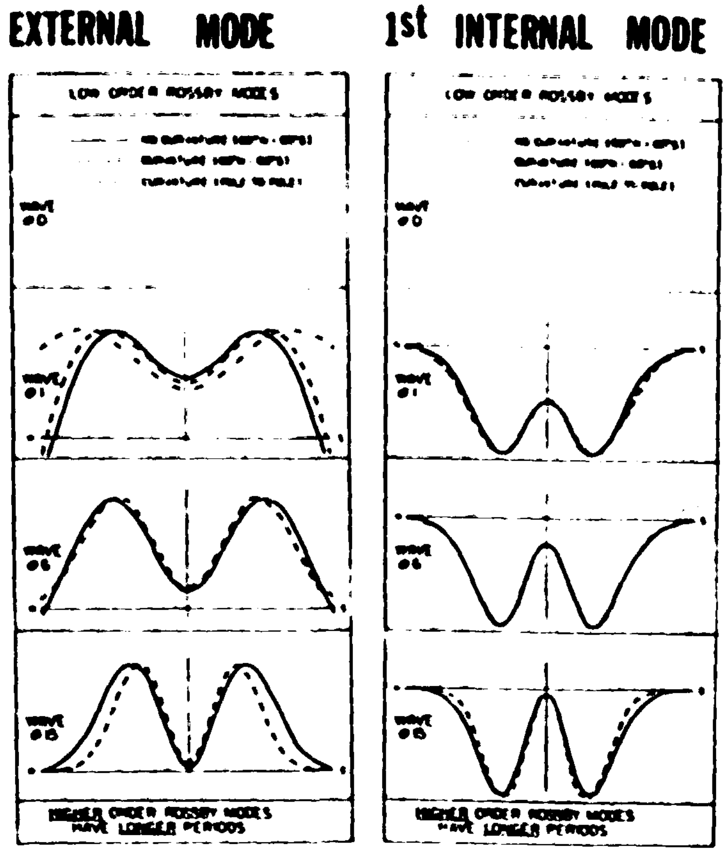

Fig. 5 Low-order Rossby modes as they depend on model geometry.

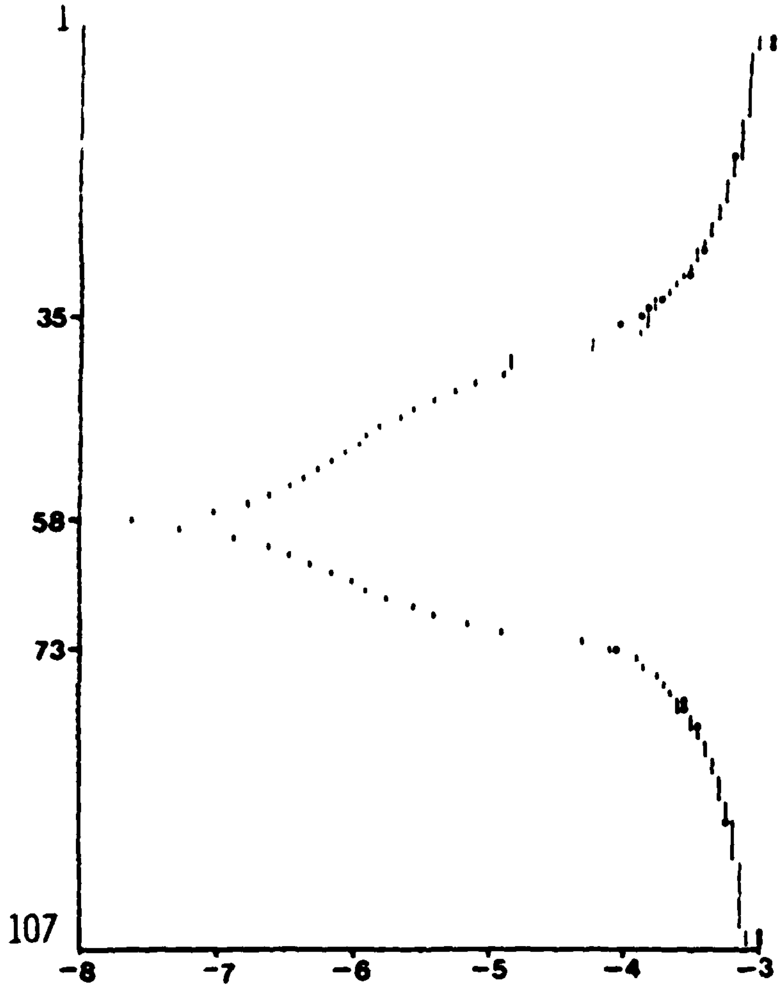

[illegible] Eigenfrequencies for longitudinal wavenumbers m = 0 and 1 with equivalent depth h = [illegible] km (external mode). The abscissa is the order of magnitude of frequency in sec^{-1}. The ordinate is the order of frequencies from the most negative (#1) to the most positive (#107). First and last 35 frequencies represent westward and eastward gravity modes, respectively. The last mode with negative frequency is #[illegible]8. There are no values in the range of Rossby modes from #36 to #72 fro m = 0. Elsewhere, if neighboring values are too close, only one of them is plotted.

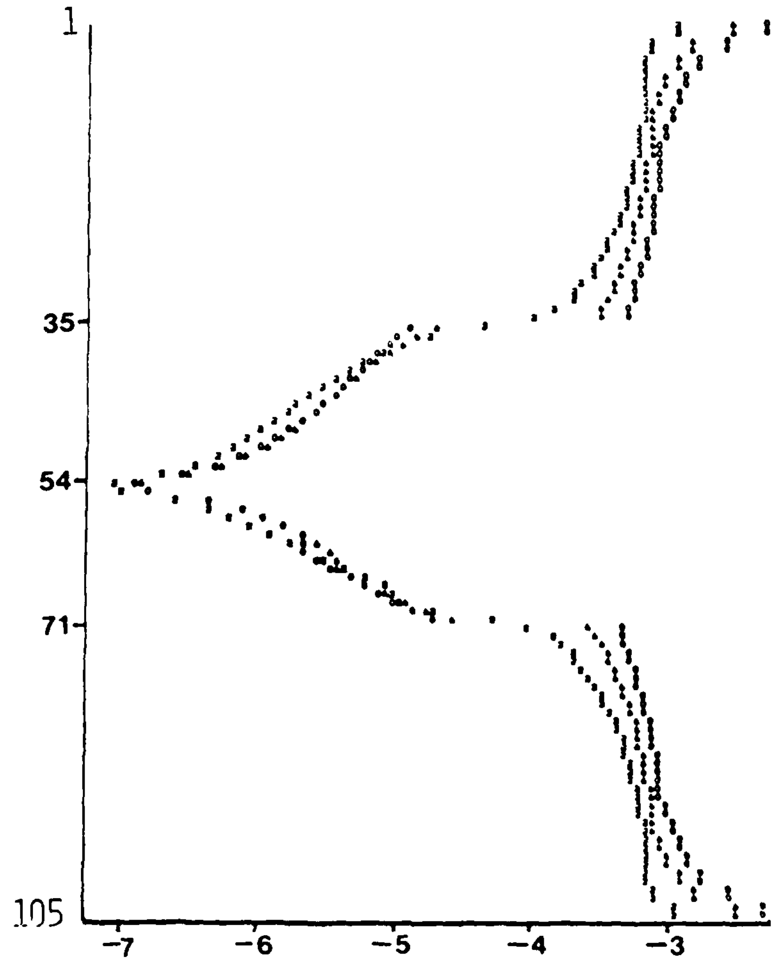

Fig. 7 Same as Fig. 6 except for m [illegible] are used for m [illegible].

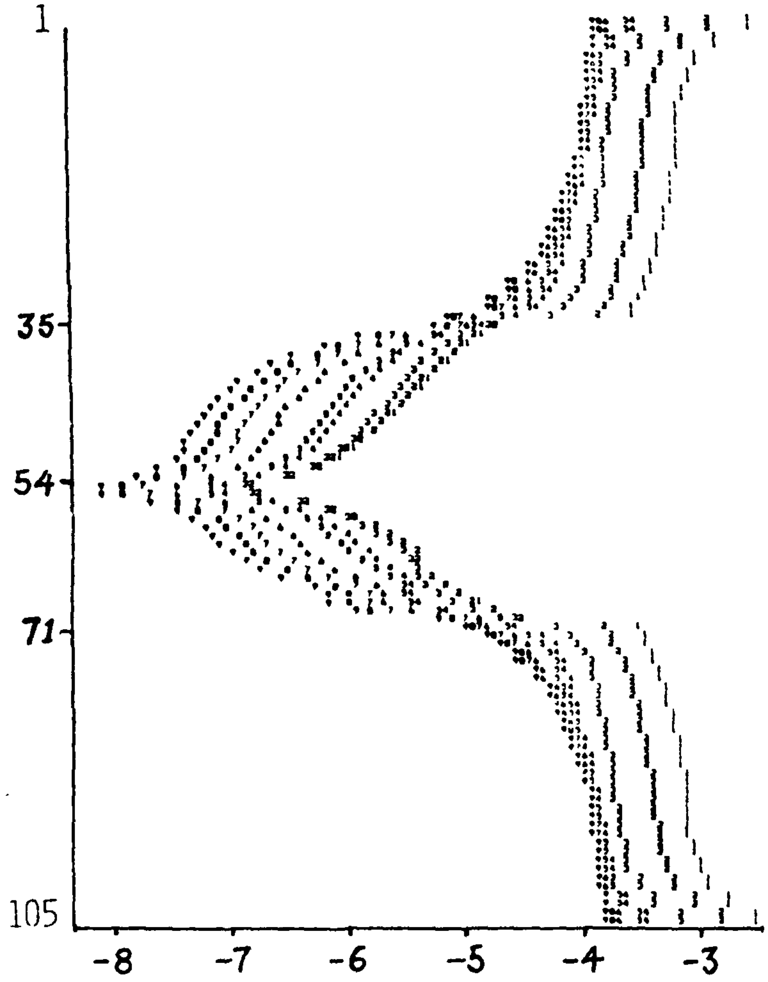

Fig. 8 Same as Fig. 6 except for m = 6. Frequencies for all 9 equivalent depths are plotted (finite difference).

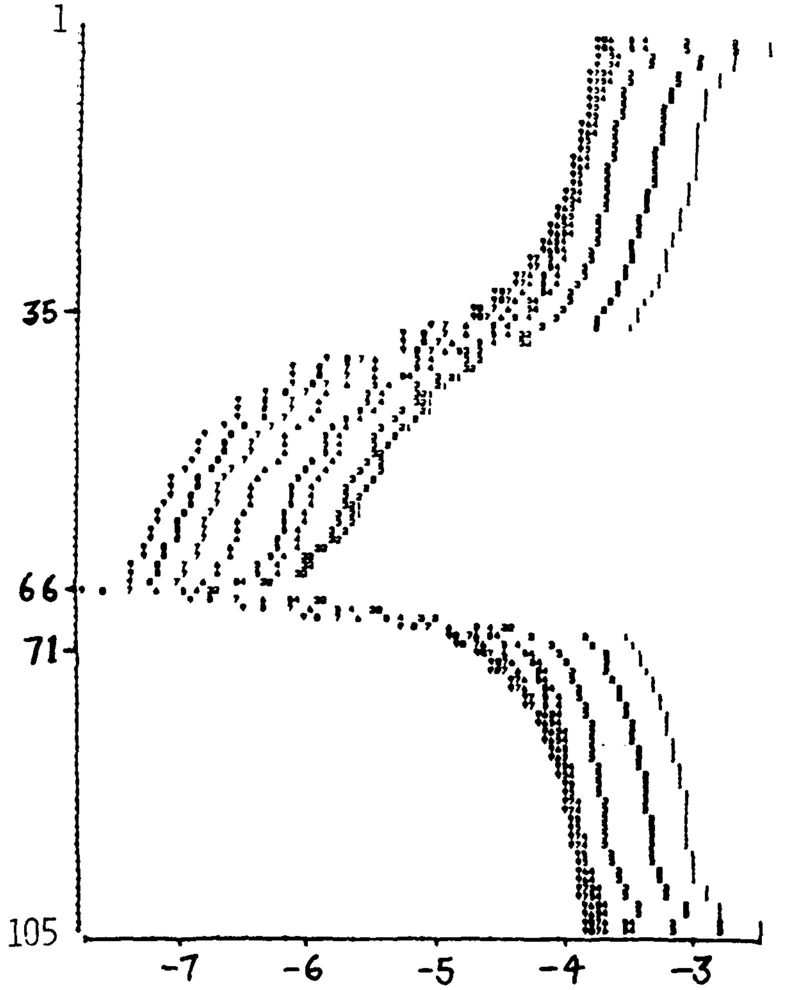

Fig. 9 Same as Fig. 8 except that the finite element method is used to establish the eigenproblem. Notice that there are more negative and relatively less positive Rossby modes than for the finite difference result.

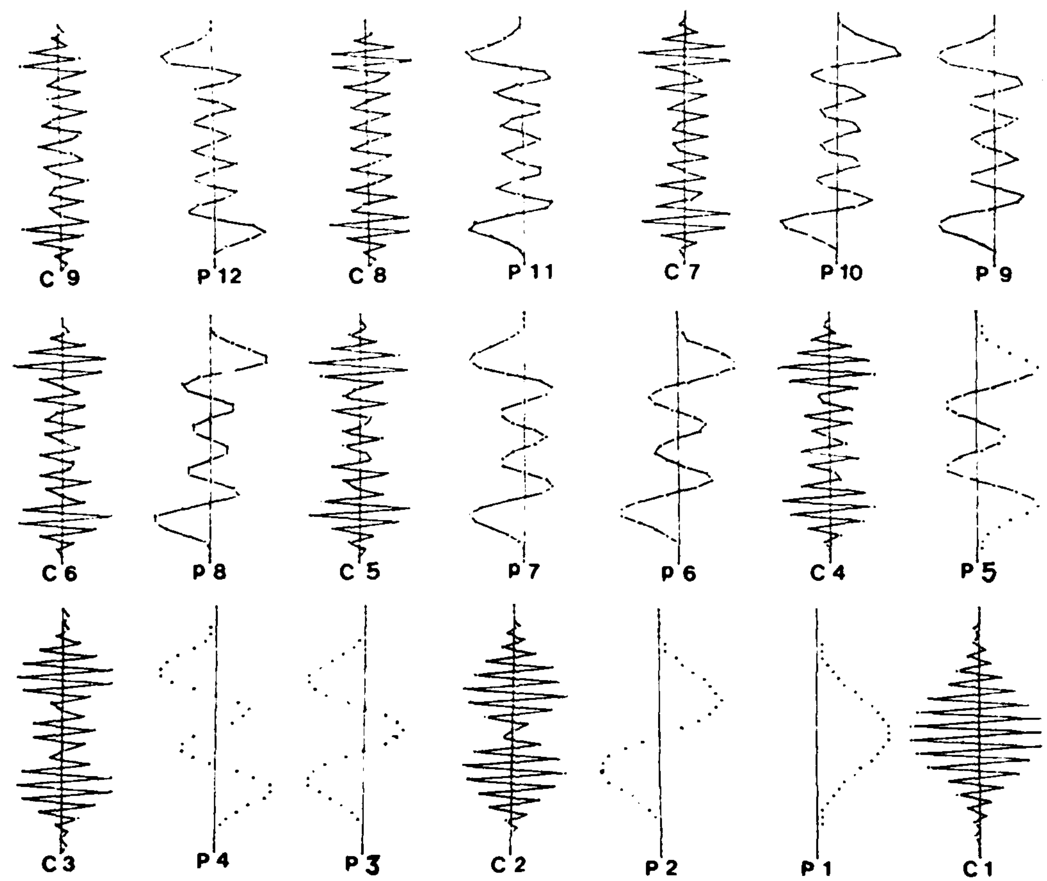

Fig. 10 Latitudinal eigenstructures of u for m = 6 and equivalent depth 9.555 km. Shown are westward gravity modes from #21 to #35, each plotted from pole-to-pole at a 5° increment. Whether a mode is computational or physical is denoted by a c or a p and they are sequenced.

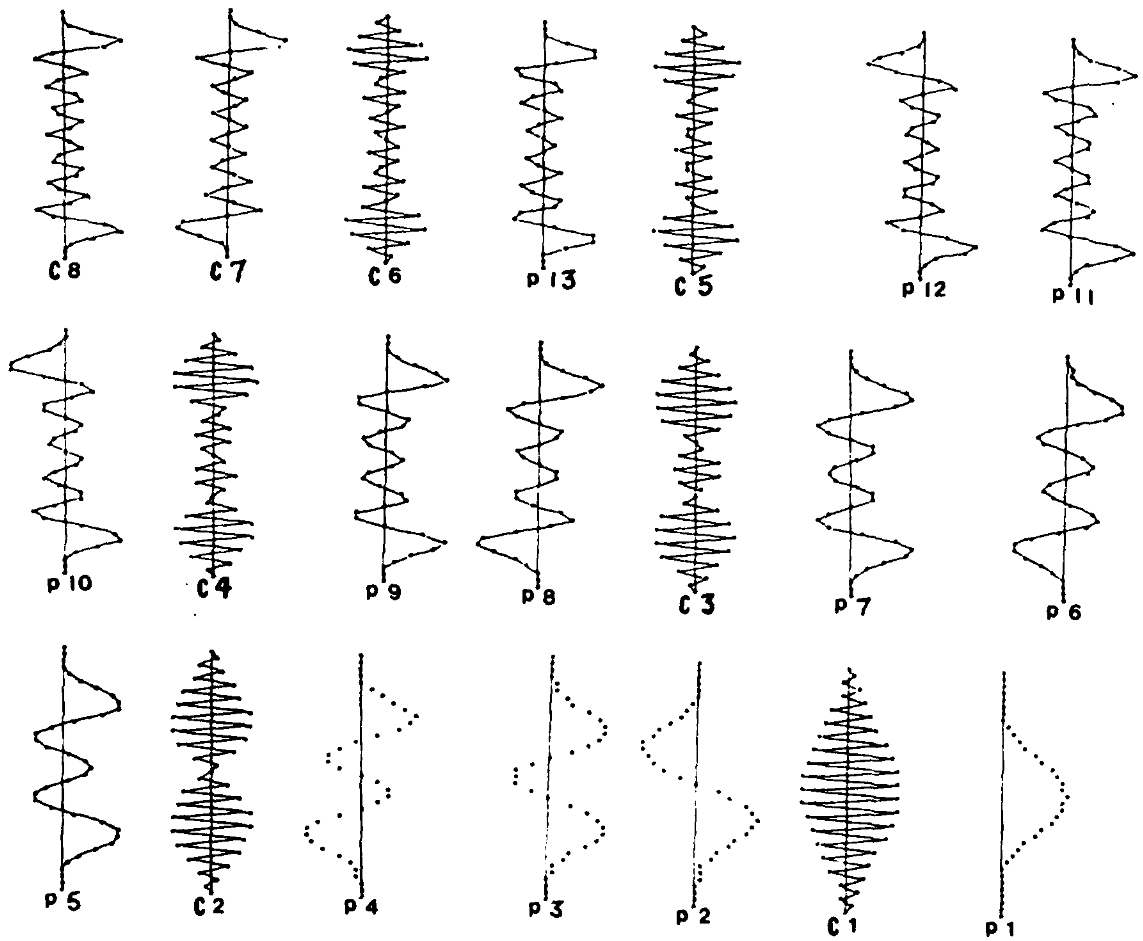

Fig. 11 Same as Fig. 10 except for results from the finite element method.

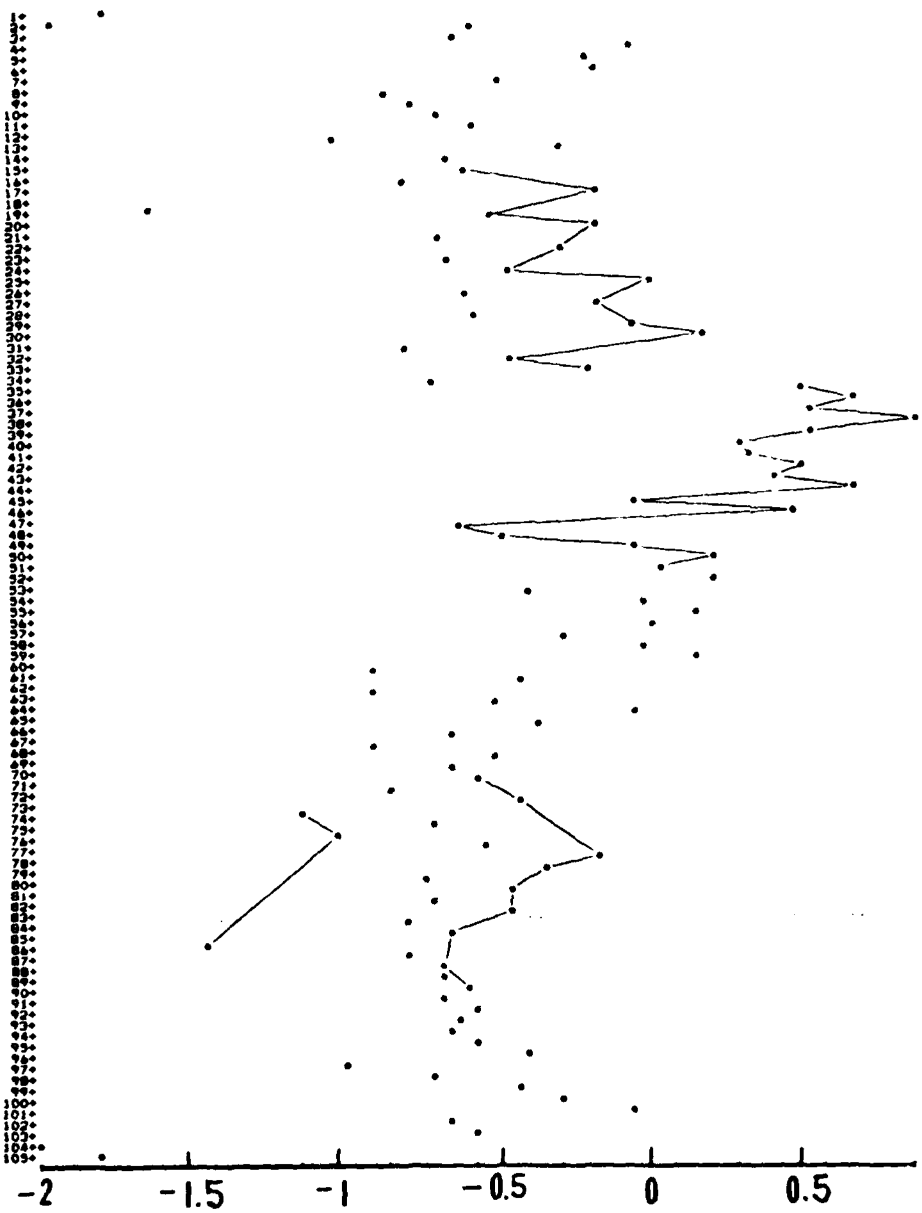

Fig. 12 Amplitudes of real data set projections onto the latitudinal modes of the 4th order difference model for $m = 6$ and equivalent depth 9.555 km. The abscissa represents order of magnitude of amplitude and the ordinate gives order number of modes. Physical modes are indicated by connecting segments.

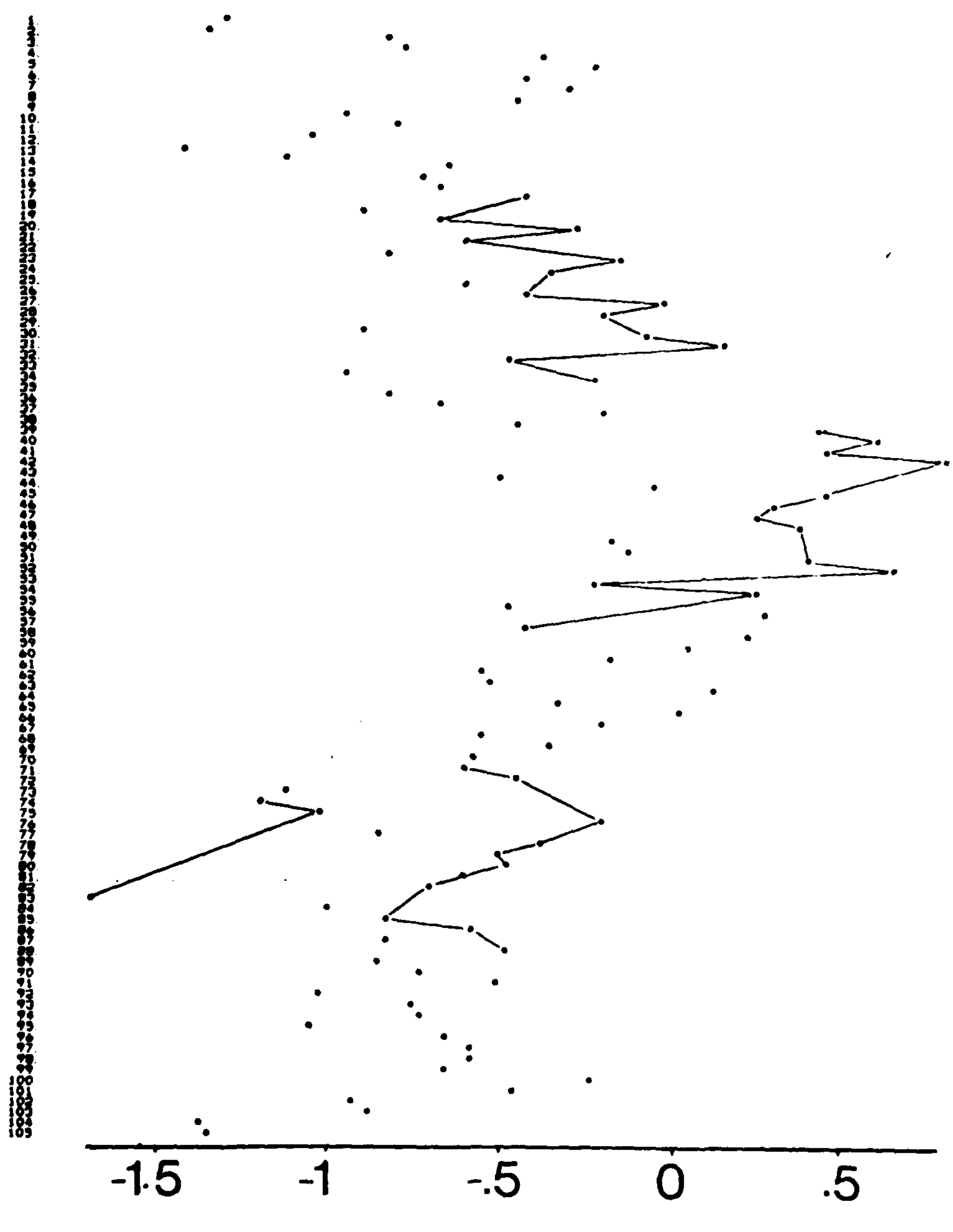

Fig. 13 Same as Fig. 12 except for the finite-element model modes.

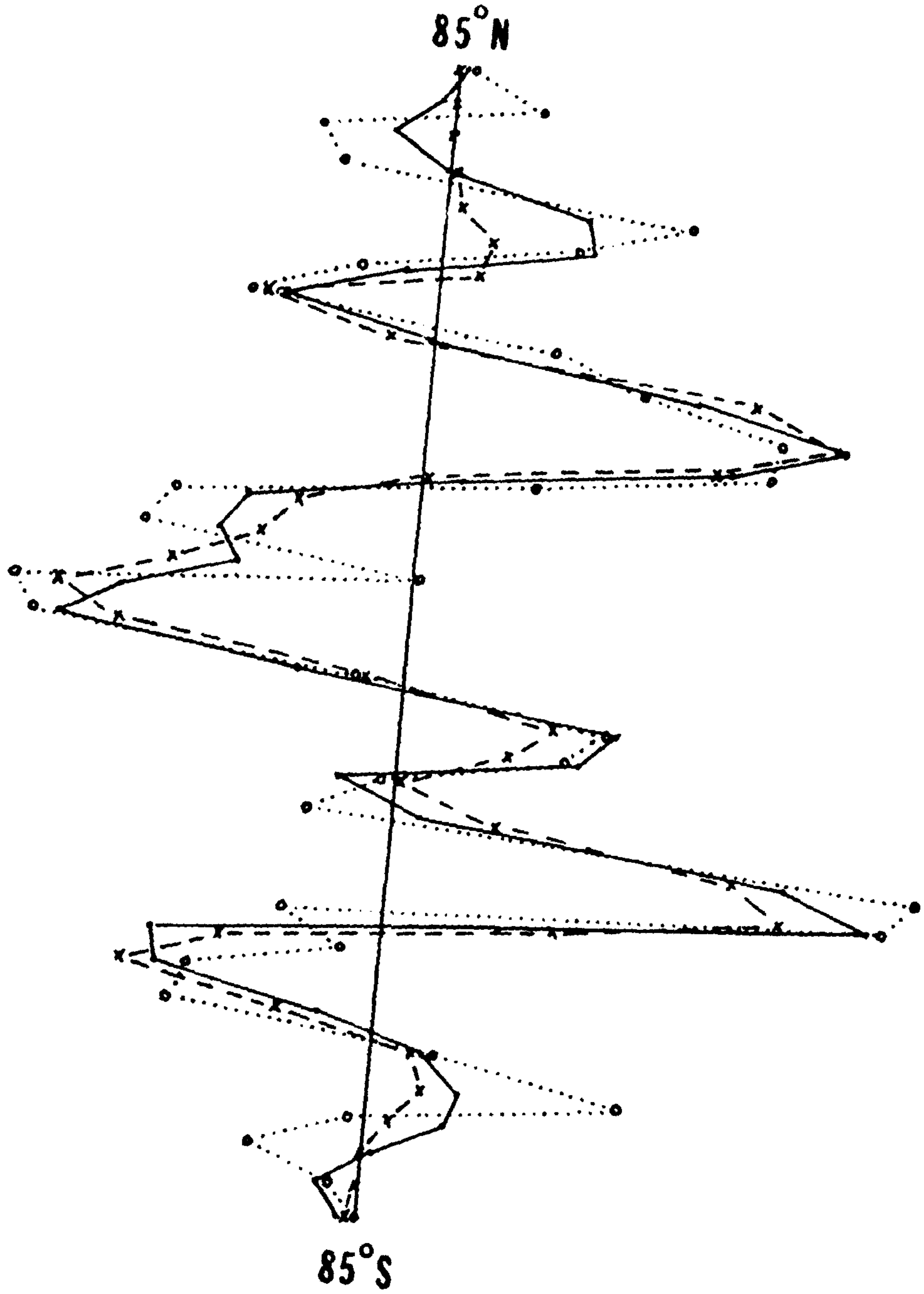

Fig. 14 Comparison of original and reconstructed latitudinal profiles. Dotted line is the real part of observed u after projecting onto the first (external) vertical mode for m = 6. Solid line is the reconstructed profile by removing amplitudes of computational modes using the finite difference method for normal mode analysis. Broken line is the reconstructed profile based on filtering with the finite element modes.

DAT
FILM
5